

# **Thermally Induced Reduction of the Load (TIRL) during Electron Beam Welding of CuCr1Zr**

**Ricardo Miguel Diogo de Oliveira Chin**

Thesis to obtain the Master of Science Degree in

## **Mechanical Engineering**

Supervisors: Prof. Inês da Fonseca Pestana Ascenso Pires  
Prof. Susana Margarida da Silva Vieira

### **Examination Committee**

Chairperson: Prof. Carlos Baptista Cardeira  
Supervisor: Prof. Susana Margarida da Silva Vieira  
Member of the Committee: Prof. Pedro Santos da Graça Effertz

**October 2021**



Dedicated to my family...



## Acknowledgments

I would like to express my sincere acknowledgements to everyone whose input has proved invaluable in my endeavour. I would like to begin by thanking prof. Dra. Susana Margarida da Silva Vieira, prof. Dra. Inês da Fonseca Pestana Ascenso Pires and prof. Dra. Maria Luísa Coutinho Gomes de Almeida for making this unexpected, but fulfilling experience possible, without them none of this would have happened. I would also like to express extreme gratitude to prof. Dr. Norbert Enzinger for giving me insightful feedback on every discussion, without whose guidance and encouragement this work would not have been achievable. I want to express my sincere thanks to prof. Dr. Pedro Santos da Graça Effertz for being my supervisor during my stay in Austria, for all the intelligent discussions he provided, for all his life advices and for being the support system I never knew I needed. I feel privileged to have worked with such a brilliant and phenomenal person.

I would also like to express appreciation to my fellow IMAT researchers at the Steyrergasse office, Mustafa Tümer and Omar Assem for providing me with a lot of insight regarding electron beam welds as well as for all the extensive coffee break debates.

I am grateful to my colleagues at Técnico namely Henrique Furtado, João Encarnação, João Moura and Pedro Ramalho for their everlasting friendship and for making the good times even better and the hard times a whole lot easier. Thank you for enrolling in this enriching adventure with me. I would also like to thank my friends at Graz - my housemate Paweł Pomierski for all our fruitful discussions that always turned into laughter. My running partner Liesl Sebrechts for being incredibly supportive, understanding my struggles and motivating me to push through every barrier. The one with the boosters Anna Köpke for the countless times she delivered unrequested support for my work and last, but certainly not least, the always smiling Anna Lindner for all our philosophical late-evening long walks that are still so present in my mind. I will treasure all these memories for the rest of my life.

Finally, I could not have achieved anything without the loving and unconditional support of my parents, sister and grandmother who never left my side and whose constant encouragement gave me all the necessary strength to break through any obstacle allowing me to accomplish my academic pursuits successfully.



## Resumo

A soldadura por feixe de elétrons é um processo de soldadura altamente eficiente e preciso que está a ser cada vez mais usado no fabrico industrial e é de notar a sua importância crescente na indústria nomeadamente devido à sua grande penetração, pureza metalúrgica da solda, baixa entrega térmica, pequena zona termicamente afetada (HAZ) e baixa susceptibilidade a deformação. Neste estudo, fissuração a quente por soldadura de feixe de elétrons (EBW) de uma geometria cilíndrica de CuCr1Zr foi investigada. Para analisar e evitar a ocorrência de fissuras a quente, um modelo numérico termo-mecanicamente acoplado foi construído usando o método de elementos finitos (FEM). Uma fonte de calor adicional foi considerada por forma a influenciar o estado de tensão residual resultante, nomeadamente para minimizar as tensões de tração na zona de fusão durante a solidificação pela introdução de tensões de compressão. Assim, uma fiscalização sistemática de parâmetros relevantes, como a densidade de potência e a posição entre as duas fontes de calor foi realizada individualmente usando o método de análise de sensibilidade *one factor at a time* (OFAT), onde apenas um parâmetro é variado deixando os restantes constantes. A influência conjunta dos parâmetros do processo foi avaliada usando as ferramentas estatísticas tais como: *Design of Experiments* (DoE) no Minitab 19 e o algoritmo de aprendizagem supervisionada *Support Vector Machine* (SVM). Foi descoberto que, para uma configuração de parâmetros específica, a fissuração a quente pode ser evitada.

**Palavras-chave:** Soldadura por feixe de elétrons, Fissuração a quente, CuCr1Zr, Método de elementos finitos, Design of experiments, Fonte de calor secundária





## Abstract

Electron Beam Welding (EBW) is a highly efficient and precise welding method that is being increasingly used in industrial manufacturing and is of growing importance in industry namely due to a greater penetration depth, metallurgical purity of the weld, low heat input, small Heat Affect Zone (HAZ) and low susceptibility to deformation. In the present study, solidification cracking in EBW of a CuCr1Zr cylindrical geometry was investigated. To analyze and avert occurrence of hot cracking, a thermomechanically coupled numerical model was built using a Finite Element Method (FEM). An additional heat source was considered in order to influence the resulting residual stress state, namely to minimize tensile stresses in the fusion zone during solidification by introducing compressive stresses. Hence, a systematic examination of relevant parameters, such as the power density and the position between both heat sources was performed individually using the sensitivity analysis method One Factor at a Time (OFAT), where only one parameter varied leaving the remaining constant. The combined influence of process parameters was assessed using the statistical tools such as: *Design of Experiments* (DoE) in Minitab 19 and the supervised learning algorithm *Support Vector Machine* (SVM). It was found that for a specific parameter configuration, solidification cracking most likely can be avoided.

**Keywords:** Electron beam welding, Hot cracking, CuCr1Zr, Finite element method, Design of experiments, Secondary heat source



# Contents

Acknowledgments . . . . .	v
Resumo . . . . .	vii
Abstract . . . . .	ix
List of Tables . . . . .	xv
List of Figures . . . . .	xvii
Nomenclature . . . . .	xxi
Glossary . . . . .	xxiii
<b>1 Introduction</b>	<b>1</b>
1.1 Motivation . . . . .	1
1.2 Problem Description . . . . .	2
1.3 Objectives . . . . .	3
1.4 Reading Guide . . . . .	4
<b>2 Electron Beam Welding</b>	<b>5</b>
2.1 Process . . . . .	5
2.2 Weld Pool Forces . . . . .	8
2.3 Process Parameters . . . . .	10
2.4 Desirable Features of EBW . . . . .	13
2.5 Undesirable Features of EBW . . . . .	14
2.6 Material . . . . .	15
2.6.1 Copper . . . . .	15
2.6.2 Weldability of Cu-alloys . . . . .	16
2.6.3 Weldability of CuCr1Zr . . . . .	17
<b>3 Finite Element Method (FEM)</b>	<b>19</b>
3.1 Tetrahedral Elements . . . . .	19
3.2 Hexahedral Elements . . . . .	20
3.3 Symmetry . . . . .	21
3.4 Heat Transfer . . . . .	21
3.5 Finite Element Analysis (FEA) . . . . .	23
3.6 Heat Source Model . . . . .	23

<b>4</b>	<b>Design of Experiments (DoE)</b>	<b>26</b>
4.1	Linear Regression (LR)	26
4.2	Least Squares Method (LSM)	27
4.2.1	Properties of the Least Square Estimator	27
4.2.2	Confidence Intervals for the Least Squares Estimator	28
4.3	Analysis of Variance (ANOVA)	29
4.4	Model Selection and Evaluation	31
4.5	Classical Designs	33
4.5.1	Full Factorial Design (FFD)	33
4.5.2	Fractional Factorial Design	34
4.5.3	Central Composite Design (CCD)	34
<b>5</b>	<b>Support Vector Machine (SVM)</b>	<b>35</b>
5.1	Linear SVM	37
5.2	Nonlinear SVM	39
5.3	Tuning Parameters	40
<b>6</b>	<b>Proposed Method</b>	<b>41</b>
6.1	Low Stress No Distortion (LSND)	41
6.2	Multi Beam Technique	42
6.3	Thermally Induced Reduction of the Load (TIRL)	43
6.4	Methodology	44
6.4.1	Secondary Heat Source (SHS)	44
6.4.2	One Factor at a Time (OFAT)	45
6.5	Numerical Implementation	47
6.5.1	Geometry Discretization	47
6.5.2	Material Properties	49
6.5.3	Heat Source Model	50
<b>7</b>	<b>Results and Discussion</b>	<b>53</b>
7.1	No Secondary Heat Source	54
7.1.1	Numerical	54
7.1.2	Experimental	55
7.2	One Factor at a Time (OFAT)	58
7.3	Design of Experiments (DoE)	60
7.4	Verification and Validation	68
7.5	Support Vector Machine (SVM)	70
<b>8</b>	<b>Conclusions</b>	<b>75</b>
8.1	Achievements	75
8.2	Undergoing and Future Work	76

<b>Bibliography</b>	<b>77</b>
<b>A Technical Datasheets</b>	<b>81</b>
A.1 EB Machine . . . . .	81



# List of Tables

2.1	Electron properties. . . . .	6
2.2	CuCr1Zr chemical composition in % [22]. . . . .	15
2.3	CuCr1Zr thermophysical properties at 20°C [23]. . . . .	15
2.4	CuCr1Zr mechanical properties at 20°C [23]. . . . .	15
6.1	Domain discretization. . . . .	48
6.2	CuCr1Zr vs. Cu_SW properties at 20°C. . . . .	49
6.3	Temperature dependent proof stress of Cu_SW. . . . .	50
6.4	MHS parameters. . . . .	50
6.5	MHS Simufact parameters. . . . .	51
6.6	Numerical calibration of process efficiency. . . . .	51
7.1	3-level full factorial DoE with 4 factors. . . . .	61
7.2	ANOVA for the initial DoE. . . . .	62
7.3	2-level full factorial DoE with 3 factors. . . . .	63
7.4	Tweaked DoE statistical results. . . . .	63
7.5	ANOVA for the modified DoE. . . . .	64
7.6	Modified DoE statistical results. . . . .	64
7.7	Solutions for the minimization of the ratio between stress and proof stress. . . . .	69
7.8	Leave-one-out cross-validation scoring results. . . . .	73
A.1	EBW-Gun benchmarks. . . . .	81
A.2	EBW-Chamber benchmarks. . . . .	81
A.3	EBW-Vacuum benchmarks. . . . .	81





# List of Figures

1.1	Sketch of the welding configuration. . . . .	2
1.2	Top view of the welding configuration. . . . .	2
2.1	EBW schematic representation [6]. . . . .	6
2.2	Coulomb force [8]. . . . .	6
2.3	Lorentz force [8]. . . . .	6
2.4	Thermal distribution of an electron beam (a) heating without melting, (b) melting without deep penetration, (c) deep penetration [8]. . . . .	8
2.5	Creation of keyhole [10]. . . . .	8
2.6	Forces acting on the EBW keyhole [10]. . . . .	9
2.7	(a) Scheme of the welding procedure, (b) Representation of the material states and fluid flow in the molten pool during the welding process [11]. . . . .	9
2.8	Schematic representation of focus length, distance, point and working distance. . . . .	10
2.9	Different focal positions. Over, ideally and under focused [15]. . . . .	11
2.10	Display of beam current over time during EBW [14]. . . . .	11
2.11	Geometries of beam oscillation [17]. . . . .	12
2.12	Different types of welding defects [24]. . . . .	16
2.13	Hot crack in a welded joint [27]. . . . .	17
2.14	Schematic view of hot cracking [8]. . . . .	17
2.15	CuCr1Zr solidification curve. Solid fraction (fs) over temperature. [25] . . . . .	18
3.1	A single tetrahedral finite element. . . . .	20
3.2	Heat source models: (a) disk source, (b) double ellipsoid source and (c) conical source [34]. . . . .	24
3.3	Detailed 3D conical heat source [35]. . . . .	25
5.1	SVM Hyperplanes between two classes. . . . .	36
5.2	Bounding planes, support vectors and maximum Margin in SVM [49]. . . . .	36
5.3	Misclassification in SVM [49]. . . . .	37
6.1	Residual stresses comparison [3]. . . . .	41
6.2	EBW with multi-beam preheating [51]. . . . .	42
6.3	Illustration of the TIRL mechanism [53]. . . . .	43

6.4	Sketched top view representing the TIRL mechanism. . . . .	43
6.5	SHS parameters. . . . .	44
6.6	Flowchart depicting the methodology implemented to define the working range of process parameters. . . . .	45
6.7	Hollow cylinder geometry. . . . .	47
6.8	Transverse cut of the geometry. . . . .	48
6.9	Flow curves for Cu_SW. . . . .	49
6.10	Experimental weld dimensions. . . . .	50
6.11	Numerical weld dimensions. . . . .	52
7.1	Thermomechanical simulation in Simufact Welding. . . . .	53
7.2	Top view on point selection. . . . .	54
7.3	Temperature over time on the surface of a pre-select point in the weld line. . . . .	54
7.4	Experimental setup. . . . .	55
7.5	Experimental thermal distribution. . . . .	56
7.6	Stress evaluation over time on the surface of a pre-selected point in the weld line. . . . .	57
7.7	Ratio between stress and proof stress over time on the surface of a pre-selected point in the weld line. Dashed line represents case of hot cracking. . . . .	57
7.8	Numerical fusion zone for the starting condition. . . . .	58
7.9	Numerical fusion zones for different power values using OFAT approach. . . . .	59
7.10	Ratio between stress and proof stress over time for different radial distances using OFAT method. Dashed line displays case of hot cracking. . . . .	59
7.11	Ratio between stress and proof stress over time for two tangential distances using OFAT method. Dashed line represents case of hot cracking. . . . .	60
7.12	Pareto chart for the standardized response of the initial DoE for $\alpha = 5\%$ . . . . .	61
7.13	Fitted means for each factor for the initial DoE. . . . .	62
7.14	Influence on the response based on the interactions between factors for the initial DoE. . . . .	62
7.15	Pareto chart for the standardized response of the tweaked DoE for $\alpha = 5\%$ . . . . .	63
7.16	Pareto chart for the standardized response of the modified DoE for $\alpha = 5\%$ . . . . .	64
7.17	Fitted means for each factor for the modified DoE. . . . .	65
7.18	Response vs. P. dt — <b>Held value</b> d = 2,25 mm. . . . .	65
7.19	Response vs. d. dt — <b>Held value</b> P = 47,5%. . . . .	66
7.20	Response vs. P. d — <b>Held value</b> dt = 3,25 mm. . . . .	66
7.21	Response vs. P. dt — <b>Held value</b> d = 2 mm. . . . .	67
7.22	Response vs. d. dt — <b>Held value</b> P = 50%. . . . .	67
7.23	Response vs. P. d — <b>Held value</b> dt = 3 mm. . . . .	68
7.24	Visual representation of the peak temperature at different times. . . . .	69
7.25	Stress evaluation over time on the surface of a pre-selected point with and without TIRL. Dashed line indicates case of hot cracking. . . . .	70

7.26 Stress/proof stress ratio for all considered data samples. . . . .	71
7.27 Cracking condition for all considered data samples. . . . .	71
7.28 Confusion matrix. . . . .	72
7.29 Leave-one-out cross-validation. . . . .	73
8.1 Support vector machine vs. Random forest . . . . .	76
A.1 EB-Machine at TU Graz. . . . .	82



# Nomenclature

## Greek symbols

$\alpha$	Angle
$\epsilon$	Error term
$\eta$	Process efficiency
$\kappa$	Thermal conductivity coefficient
$\omega$	Angular velocity
$\rho$	Density
$\sigma$	Stress
$v$	Welding velocity

## Roman symbols

$\mathbf{u}$	Velocity vector
$f$	Focal position
$v$	Velocity
$D$	Diameter
$d$	Radial distance
$d_0$	Focal point
$d_c$	Heat source conical depth
$dt$	Tangential distance
$E$	Energy
$f$	Fraction of power
$I_B$	Beam current
$L_f$	Focus distance

$L_w$	Electron beam working distance
$M$	Gaussian parameter
$m$	Mass
$P$	Power
$Q$	Heat input
$q$	Rate of heat
$r$	Radius
$r_l$	Heat source lower radius
$r_u$	Heat source upper radius
$R_{Pr}$	Penetration depth
$T$	Temperature
$t$	Time
$U_B$	Accelerating voltage

### Subscripts

$e$	Element
$i, j, k$	Computational indexes
$n$	Normal component
$x, y, z$	Cartesian components
$L$	Liquidus
ref	Reference condition

### Superscripts

$T$	Transpose
-----	-----------

## **Glossary**

**ANOVA** Analysis of Variance

**CAD** Computer Aided Design

**CCD** Central Composite Design

**DC-LSND** Dynamically Controlled Low Stress No Distortion

**DoE** Design of Experiments

**DoF** Degrees of Freedom

**EBW** Electron Beam Welding

**FEA** Finite Element Analysis

**FEM** Finite Element Method

**FFD** Full Factorial Design

**HAZ** Heat Affected Zone

**ISO** International Organization for Standardization

**LBW** Laser Beam Welding

**LR** Linear Regression

**LSM** Least Squares Method

**LSND** Low Stress No Distortion

**MHS** Main Heat Source

**OFAT** One Factor At a Time

**RBF** Radial Basis Function

**SHS** Secondary Heat Source

**SSE** Sum of Squares of Errors

**SSR** Sum of Squares due to Regression

**SST** Total Sum of Squares

**SVM** Support Vector Machine

**TIRL** Thermally Induced Reduction of the Load





# Chapter 1

## Introduction

### 1.1 Motivation

EBW remains indispensable in many aerospace, biomedical and mechanical industries specifically due to a greater penetration depth, metallurgical purity of the weld, low heat input, small HAZ and a rather small deformation susceptibility. Over the past decade significant developments in modelling and simulation of the thermal cycle and the subsequent mechanical behaviour became very limited due to the inherent complexity of boundary conditions and the nonlinearity of material properties [1]. For years, analytical, numerical and empirical approaches have been employed in this regard either separately or in combination. Analytical solutions are generally the exact and fast solutions of differential equations considering simplified boundary conditions and constant material properties. Therefore, these solutions cannot be directly applied to complex manufacturing cases. The development of numerical techniques like the FEM has enabled researchers to overcome some practical difficulties such as complex boundary conditions, arbitrary geometry, and temperature dependent material properties [2]. Despite the technological innovations in FEM, there are still some problems when it comes to EBW, especially hot cracking. In order to solve this problem, other authors have tried to apply different experimental techniques, for instance, applying auxiliary heat sources on both sides of the weld to produce certain thermal gradients, and cooling elements under the weld to generate a specified temperature field altering the stresses occurring in the weld zone. However, such methodologies proved to be costly and time consuming [3], [4] creating the need for numerical studies which is exactly the goal of this thesis – a thorough numerical study on the hot cracking susceptibility in EBW of CuCr1Zr.

## 1.2 Problem Description

In the present study, solidification cracking in EBW of a revolving CuCr1Zr geometry was investigated. The goal was to weld a top lid onto an hollow cylinder around the full circle of the geometry, Figure 1.1.

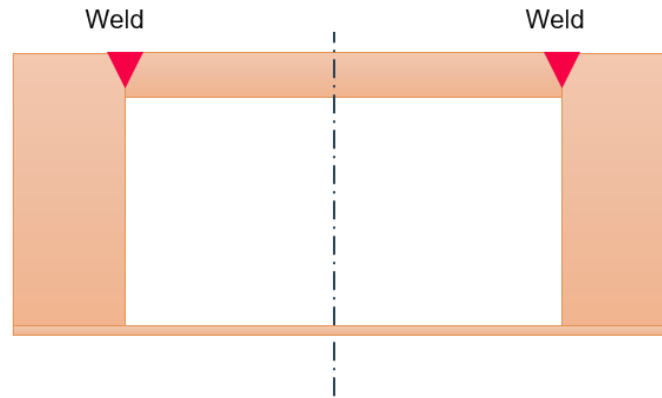


Figure 1.1: Sketch of the welding configuration.

Cracking occurred due to the high stress caused by shrinkage stresses. This configuration, in Figure 1.2, was used to investigate the susceptibility of CuCr1Zr to hot cracking. In this case, the damage was undesirable leading to the rejection of many parts and increasing the company's cost.

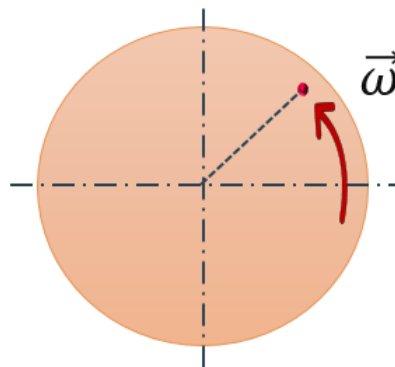


Figure 1.2: Top view of the welding configuration.

## 1.3 Objectives

The objectives for this work are based on the problem exposed previously in Subsection 1.2 and are:

- To understand the advantages of employing electron beam welding process relatively to other commonly used processes;
- To investigate the importance of knowing residual stress state present in a component;
- To acknowledge how the stress field is correlated with the occurrence of a critical weldability issue: hot cracking;
- To propose a feasible methodology that could nullify occurrence of hot cracking;
- To build a thermomechanical model in Simufact Welding for analyzing structural integrity;
- To select which process parameters are more influential in altering the residual stress state;
- To apply statistical tools using Minitab 19 for process parameter configuration optimization;
- To verify and validate that it is possible to avert hot cracks in CuCr1Zr by means of EBW.

## 1.4 Reading Guide

This section contains a brief description of the main topics covered in this dissertation. Primarily, the literature review in Chapter 2 aims to provide an extended explanation on how the electron beam process operates. This chapter is divided in sections: 1) a brief analysis on the process and 2) the forces acting on the weld pool; Section 3) describes the vast majority of the process parameters, followed by 4) where desirable and 5) undesirable features arising from the process itself are described. Lastly, a dense section 6) describing the material used and the state-of-the-art regarding conducted experiments with this specific copper alloy. The critical problem of this thesis, hot cracking, is also thoroughly addressed.

Chapter 3 introduces the topic of FEM, where different types of elements are depicted as well as the finite element analysis based on the thermal loads. The heat source model is also descriptively analyzed. In chapter 4, it is given a brief introduction on statistics tool DoE. Furthermore, topics such as linear regression, method of least squares and Analysis of Variance (ANOVA) are also covered. A different alternative using supervised machine learning algorithms is presented in Chapter 5.

In Chapter 6, existent solutions to avert occurrence of hot cracking are displayed and a proposed method is shown. A methodology is also suggested involving the One Factor at Time method (OFAT) and DoE. A theoretical criteria for avoidance of hot cracks is presented. At the end, the numerical implementation of the methodology is explained: the geometry discretization, material properties and the heat source model.

Chapter 7 clarifies how it is possible to extract valuable data from the numerical implementation conducted in Chapter 5. It also indicates how the data is post-processed and, finally, the results are discussed accurately.

Ultimately, the achievements and future work relevant in the scope of this thesis are presented in Chapter 8.

## Chapter 2

# Electron Beam Welding

This chapter aims to provide a theoretical background on EBW. It consists on adding important notions about notorious topics such as how the process works, the process parameters and how the forces are correlated with the welding phenomenon. At the end, some important advantages are presented as well as few downsides of using EBW making the use of numerical simulations of great interest.

### 2.1 Process

EBW is a fusion welding process where a narrow beam of electrons with high velocity is used to weld the two pieces of metals. The work pieces melt as the **kinetic energy of the electrons** is transformed into heat upon impact. The welding is often carried out in a vacuum to prevent dispersion of the electron beam, **preserving high power density** and to avoid oxidation of the high temperature metal [5]. Due to its high energy density, it is capable of forming a deep and narrow keyhole that results in deep and narrow welds.

The heart of the electron beam process resides in the electron beam gun assembly (Figure 2.1). It starts with connecting the negative terminal of a generator or battery to a cathode, made of a negatively charged emitting material, e.g. tungsten, in order to supply free electrons.

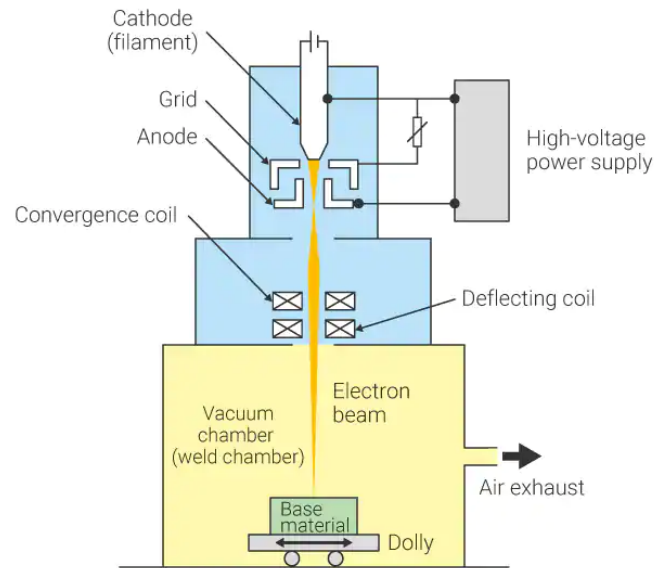


Figure 2.1: EBW schematic representation [6].

Electrons are, as protons and neutrons, elementary particles of matter. Electrons occur bonded to an atomic nucleus - free electrons in vacuum [7].

Mass (g)	Electric Charge (C)
$9,110 \cdot 10^{-28}$	$1,6021 \cdot 10^{-10}$

Table 2.1: Electron properties.

The electrons can be accelerated due to their electric charge by an electric field ( $\vec{E}$ ) and their orbit can be controlled with magnetic fields ( $\vec{B}$ ). The responsible force for acceleration is the Coulomb force while the Lorentz force affects the electrons while moving through a magnetic field. Figures 2.2 and 2.3 show the orientation of the forces due to the magnetic and electric fields.

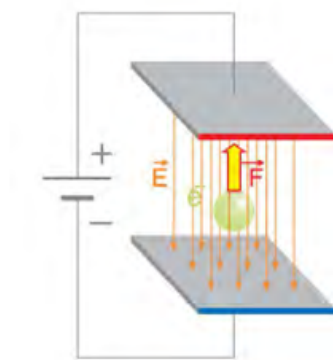


Figure 2.2: Coulomb force [8].

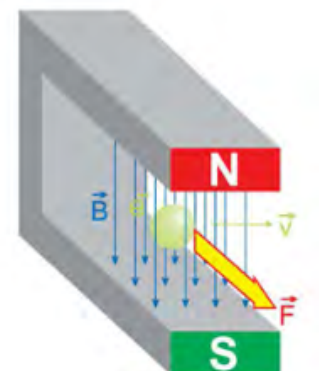


Figure 2.3: Lorentz force [8].

Electrons gain enough energy to leave the material's surface when the cathode, in a vacuum, is **sufficiently heated to its thermionic emission temperature range**. They gather around the filament and form an electron cloud. The number of the emitted electrons is correlated with the filament's temperature.

The passage is controlled through the use of a grid that is located close to the filament and is held at a negative potential in respect to it. **As the voltage potential between the filament and grid is reduced, electrons are allowed to escape.** These are then attracted to the anode, which has more positive potential than the electrons.

The anode, in the case of EBW, has a hole in its center allowing electrons to pass through as a stream and projected onto the work piece. The emitted electrons then pass a electromagnetic focusing coil so that the beam can be **appropriately focused in order to achieve enough power density** to weld different base materials.

When the emitted electron meets the surface of a solid or a liquid, it penetrates a thin layer with no significant drop in velocity before it encounters resistance from the target material and decreases its velocity. **The lower the density of the target material the deeper the electron will penetrate.** As the electrons velocity decreases, their kinetic energy, Equation 2.1, is transferred to the target material in the form of **heat**.

$$E = \frac{m \cdot v^2}{2} + \frac{3}{8} \frac{m \cdot v^4}{c^2} + \frac{5}{16} \frac{m \cdot v^6}{c^4} + \dots \quad (2.1)$$

The amount of heating and the depth of penetration that is achieved from an electron beam is dependent on the accelerating voltage (which is the initial energy of each electron), the beam current (which is the number of electrons impacting the target surface per unit time), and the density of the target material. An approximate value is given by the Equation 2.2 of Schonland - can be applied to different materials. The result specifies the distance in which the electrons lose 99% of their kinetic energy.

$$R_{pr} = 2,1 \cdot 10^2 \cdot \frac{U_B^2}{\rho} \quad (2.2)$$

At **very low power densities** the electron beam will cause only heating without any melt of the target occurring (Figure 2.4a). This function has the potential to be used for **preheating material** before welding or post weld heat treatments. As this method does not require a tightly focused beam, a defocused beam could cover a large area. At **low power densities**, caused by either a defocused beam or a low beam current, the electron beam energy is only transferred to areas near the surface of the target material. This forms shallow weld pools and the welding mode is called conduction mode welding (Figure 2.4b). The vaporisation of some of the target material is the key to deep penetration welds in electron beam welding when employing **high power densities**. The electrons can penetrate many times greater through vapour than in the solid due to the large differences in density. The vapour pressure opens up a hole in the hot zone of the weld pool allowing the beam to penetrate deeper with the potential to pass through the other side of the target material. This type of welding is called **keyhole welding** (Figure 2.4c) [9].

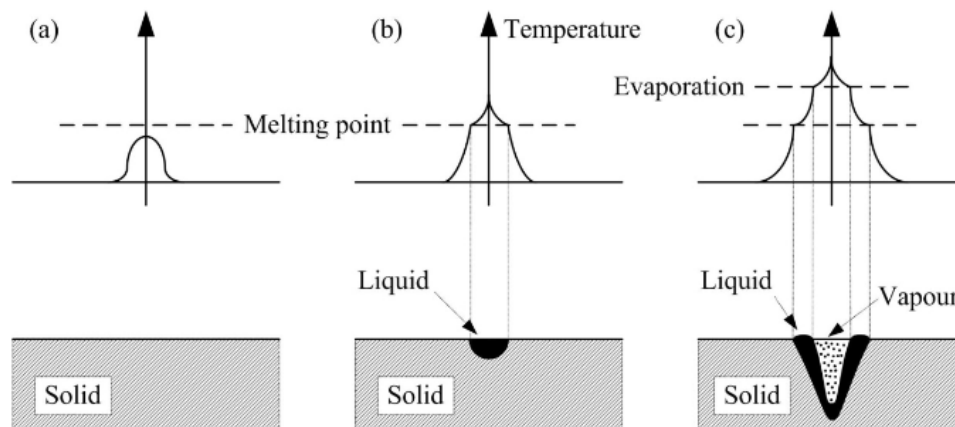


Figure 2.4: Thermal distribution of an electron beam (a) heating without melting, (b) melting without deep penetration, (c) deep penetration [8].

## 2.2 Weld Pool Forces

The incident beam of electrons hitting the work piece evaporates the underlying material and rapidly forms a metal vapor cavity, or keyhole, which is surrounded by a column of liquid metal as seen in Figure 2.6.

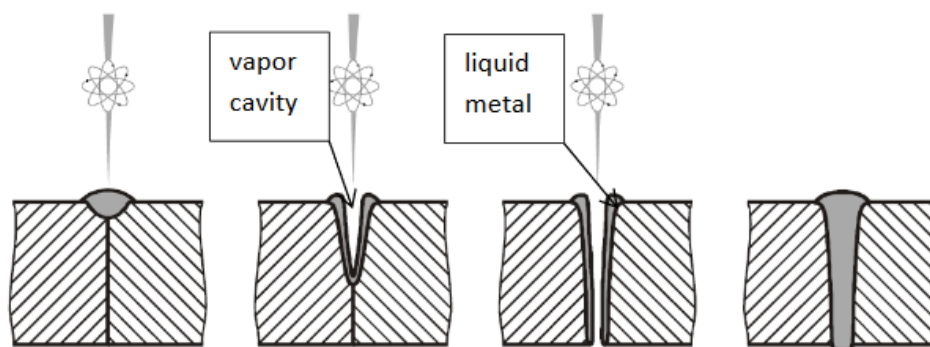


Figure 2.5: Creation of keyhole [10].

The keyhole walls remain open due to the **vapor pressure** of boiling metal. This pressure is constantly being balanced against the **hydrostatic pressure and the surface tension** of the molten column.

A schematic representation of material phases as well as a representation of forces and effects that are actuating on the weld pool is exemplified in Figure 2.7 and Figure 2.6.



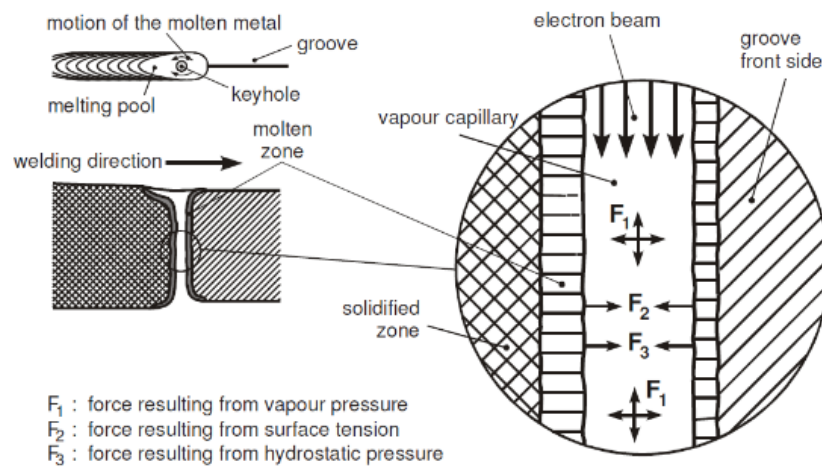


Figure 2.6: Forces acting on the EBW keyhole [10].

The vapour pressure produced by the keyhole effect needs to stay high enough to withstand the gradient of surface tension and hydrostatic pressure within the weld pool, so that the hole that was opened up can be maintained that way for as long as sufficient power is being supplied, otherwise it can collapse, resulting in some inconsistencies. In some cases, the keyhole can even be recreated by the beam which will create further turbulence. Increasing weld travel speed can lead to turbulent flow and porosity, whereas a relatively small welding travel speed increased heat transferred into base metal leading to distortion and penetration depth [10].

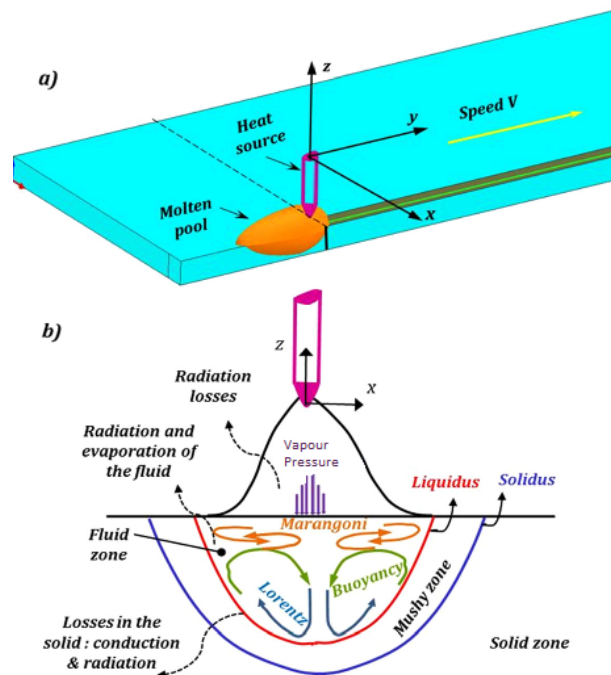


Figure 2.7: (a) Scheme of the welding procedure, (b) Representation of the material states and fluid flow in the molten pool during the welding process [11].

## 2.3 Process Parameters

EBW offers numerous adjustable parameters that will be listed based on all norms and term definitions taken from International Organization for Standardization - ISO 15609-3(EN), ISO/TR 17671-7(EN) - [12, 13]. The **repeatability and stability of the process are very high** due to the high level of machine controllability of the different process parameters. Welding experiments can be repeated exactly, given the subsequently mentioned process parameters.

- **Working Distance**

The distance,  $L_w$ , between the surface of the work-piece and a fixed reference surface of the device with a defined distance from the focus-lens center. The operating distance should be kept constant within an experiment to acquire comparable results due to the convergence of the beam.

- **Focusing Length and Focal Position**

The distance,  $L_f$ , between the focus-lens and the principal focal point of the beam,  $d_0$ , is represented in 2.8.

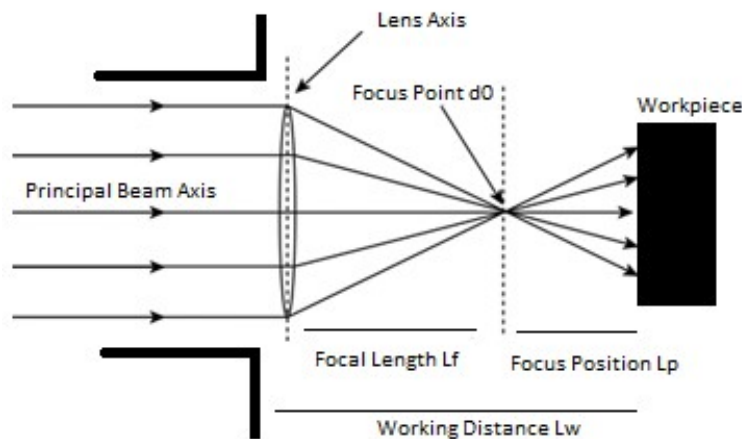


Figure 2.8: Schematic representation of focus length, distance, point and working distance.

The term focal position  $f$  (mA) is used to describe the position of the focal point of the beam at  $d_0$ , related to the position of the work piece surface [14]. This position can have a negative value if the focal point is below the surface or a positive value if it the focal point is above the surface. A better representation can be seen in Figure 2.9.

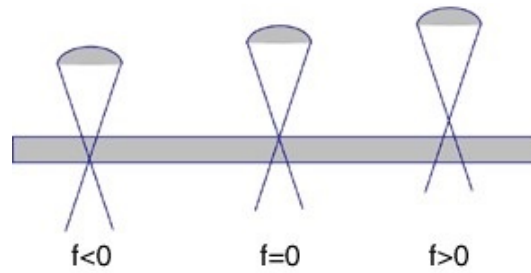


Figure 2.9: Different focal positions. Over, ideally and under focused [15].

Focus ends up being one very important parameter when it comes to welding as it is directly related with the forces actuating in the melting pool, as previously designed in Section 2.2. Defocusing is a simple yet very effective way of affecting the relationship between the forces acting in the keyhole [16].

- **Lens Current**

The current (mA) required to focus the beam.

- **Accelerating Voltage  $U_B$**

The accelerating voltage (kV) directly affects the speed of the electrons (it corresponds to the electric potential between the cathode and the anode). According to Schultz [16] it is advantageous to use a higher acceleration voltage and a low beam current to obtain a smaller beam spot diameter in the focal point. This setup is more tolerant to a change of the focal position and the machine adjustment is easier.

- **Beam Current  $I_B$**

The optimal beam current (mA) is responsible for a proper welding bead on both, face and root, sides of the welding. For a smooth start and end of the welding, the beam current is gradually raised at the beginning of the welding and gradually reduced at the end of a welding. This is called “slope-in” and “slope-out” and is shown in Figure 2.10.

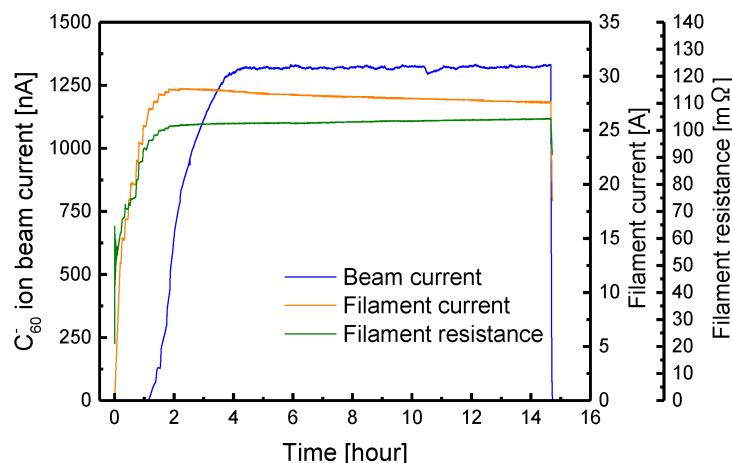


Figure 2.10: Display of beam current over time during EBW [14].

- **Beam Power  $P_B$**

The number of electrons arriving per unit time (W) is directly proportional to the beam current, so the beam power can be expressed in terms of the product of the accelerating voltage and the beam current.

$$P_B = U_B \cdot I_B \quad (2.3)$$

- **Beam Pulsation**

The beam current is not constant all the time, there are some slight variations. This periodic variation of the beam current is the beam pulsation (mA). It is noted that there is a maximum and minimum beam current and a respective frequency.

- **Beam Oscillation**

Periodic deflection of the beam by electromagnetic forces. According to Figure 2.11, a combination of different beam geometries, amplitudes, frequencies and orientations can be employed and used regarding their use for stabilization of the keyhole during welding and to smooth the top seam bead. This helps avoiding incomplete fusion, porosity that might occur in alloys with low melting points and the creation of spatter.

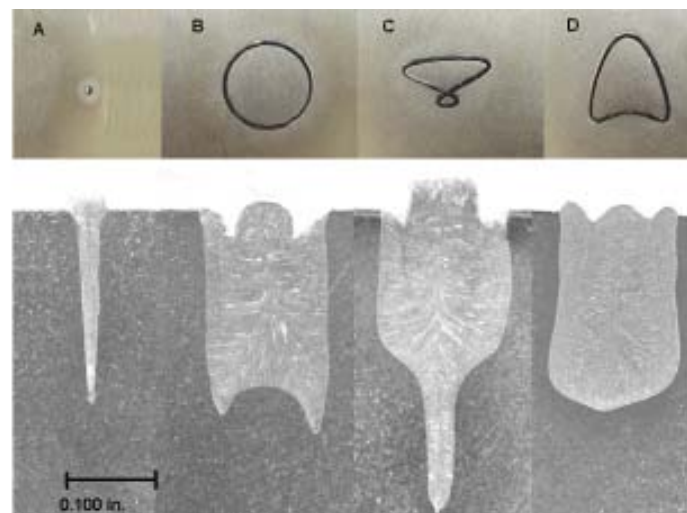


Figure 2.11: Geometries of beam oscillation [17].

- **Welding Velocity**

The relative speed of the beam (mm/s) along the workpiece [18]. It is dependent on the flow rate of the material that has to be welded and also on the thickness of the material that needs to be welded.

## 2.4 Desirable Features of EBW

It is important to highlight some features that make the EBW process more efficient over other currently available welding processes.

- **Chemical Purity**

The EBW is performed **in a high vacuum environment** where the **chemically inert electron beam** carries energy to the target material, unlike any other welding process where chemical impurities can often be seen due to the gas environment [7].

- **High Power Efficiency**

The EBW is a welding process where **nearly all the power input** into the electron gun gets transferred into heat in the target material. There are minor losses due to the formation of X rays and secondary electrons [7].

- **Controlled Guidance to Pre-selected Areas**

Being controlled by electrostatic or magnetic lenses it can be **easily deflected or focused** to rapidly guide the beams energy to predetermined positions and vary power densities rapidly [7].

- **Wide Range of Powers**

The power level can be altered by changing the beam current or the accelerating voltage. The level of variation available allows the same electron beam welding machines to be used over a large range of thicknesses, from over 150mm to as thin as 0.1mm foils [7].

- **High Power Density**

As power density is a function of area, power and time, it can be varied through control of the power output of the beam through adjustments to the beam current and accelerating voltage, or through manipulation of the beam. The beam can be defocused and spread over a large area or focused to a fine spot for a high density beam. Rapid beam oscillation and beam deflection can be used to decrease the beam density of a fine focus beam with rapid travel speeds that decrease the time the beam is in one spot [7].

- **Suitable for Electrically Conductive Materials**

Due to copper's high reflectivity, this characteristic makes EBW preferred over Laser Beam Welding (LBW).

## 2.5 Undesirable Features of EBW

Despite having great advantages, there are still some downsides when it comes to EBW. In this case, some of them create the need to conduct thermal and thermomechanical simulations.

- **Use of Vacuum**

An electron beam cannot be generated outside of a high vacuum environment. Vacuum chambers can take a **long time to pump down** which has to be factored into manufacturing times. The chamber size may limit the size or shape of the components that can be handled. Operation of low vacuum or no vacuum work chambers offer a solution to reduce or remove the long pump down times, but welds performed in this environment lose some of the benefits working in a vacuum environment can offer. A high vacuum environment is still required for the gun assembly to operate even in the low or no vacuum EBW machines. Materials like wood can be an issue in vacuum chambers, as they can slowly bleed captured gases affecting the vacuum level. This effect may limit what composite items can be electron beam welded [5, 9].

- **Radiation Hazards**

When electrons impact any surface during electron beam welding X-rays are formed. As a result of the X-ray radiation, shielding is required. Regular radiation certification is required for all machines and operators to ensure electron beam welding can be performed safely.

- **Unwanted Material Evaporation**

Materials with a high vapour pressure near their melting point will evaporate during the fusion process. If these materials are part of an alloy then composition control can become very complicated and additions may be required to compensate for the evaporation losses.

- **High Capital Cost**

Compared with traditional welding equipment the high cost for a vacuum plant and high voltage equipment makes for a significant capital outlay when setting up an electron beam welding machine [19].

- **Magnetic Fields**

Electron beams can be distorted or deflected by the presence of magnetic fields. Magnetic materials to be welded and any fixtures must be demagnetised before welding or the beam may not be able to follow the desired path. Magnetic fields can also be formed during the welding of dissimilar materials.

## 2.6 Material

### 2.6.1 Copper

Copper has outstanding electrical and heat transfer properties, moderately high-toughness and relatively high strength [20]. Other common elements are alloyed with copper to improve certain material characteristics such as corrosion resistance or machinability commonly used in a wide range of industrial applications. In this specific work, a copper alloy CuCr1Zr was used. This copper alloy contains small amount of chromium and zirconium which contribute to preserve **excellent thermomechanical** properties of copper at high temperature and **increase wear resistance**. Due to the very low solubility of Cr and Zr in copper, the thermal conductivity is still high. The excellent strength is attributed to the precipitation and particle-dispersion strengthening mechanisms [21].

Fe	Si	Cr	Zr	Other	Cu
0-0,08	0-0,1	0,5-1,2	0,03-0,3	0,2	Bal.

Table 2.2: CuCr1Zr chemical composition in % [22].

Thermophysical Properties	
Density [g/cm <sup>3</sup> ]	8,89
Melting Temperature Range [°C]	1070-1080
Thermal Conductivity [W/mK]	170
Coefficient of thermal Expansion	16,45 x 10 <sup>-6</sup> per °C
Specific heat capacity [J/ (kg.K)]	380

Table 2.3: CuCr1Zr thermophysical properties at 20 °C [23].

Mechanical Properties	
Tensile Stress [MPa]	380
Proof Stress [MPa]	300
Elongation [%]	15
Hardness Brinell [HB]	130
Young Modulus [GPa]	128
Kirchhoff's Modulus [GPa]	49,2

Table 2.4: CuCr1Zr mechanical properties at 20 °C [23].

### 2.6.2 Weldability of Cu-alloys

Welding defects can be defined as imperfections that compromise the usefulness of the welded parts. Defects in weld joints could result in the rejection of parts and assemblies, costly repairs, significant reduction of performance under working conditions and, in extreme cases, catastrophic failures with loss of property and life. Common welding defects in Cu-alloys are shown in Figure 2.12.

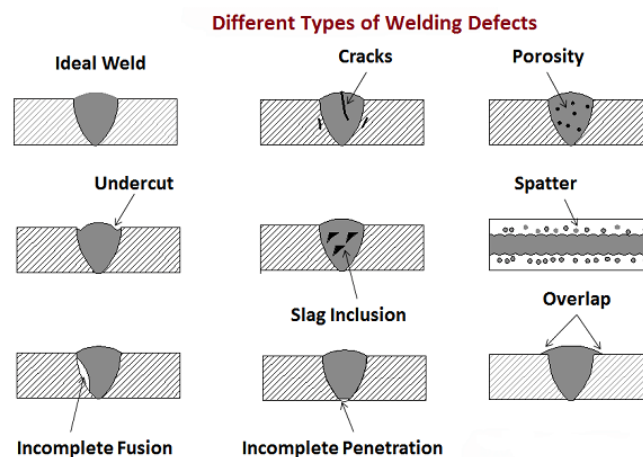


Figure 2.12: Different types of welding defects [24].

For instance, porosity is undeniably one of the most common issues occurring in copper alloys. The vaporisation during keyhole welding of elements whose boiling points are low such as zinc, cadmium and phosphorous can lead to porosity. Alloys with considerable oxygen percentage in their composition can also cause porosity and reduce strength of the welds if the quantities of deoxidizing elements, ie: manganese, are not sufficient [21].



### 2.6.3 Weldability of CuCr1Zr

Wiesniewski *et al.* [25] made experiments with EBW on thin rectangular plates of CuCr1Zr and found that **most defects were due to hot cracking**. A hot crack, represented in Figure 2.13, occurs during the latest stages of solidification due to solidification shrinkage and thermal contraction when the residual stresses emerged across neighbouring grains surpass the strength of the solidifying metal. It is mostly seen when the percentage of solid is between 80% and 90%. At this point, the movement of the remaining liquid is restricted by surface tension. As a consequence of this entrapment in between interlocking dendrites, continuous liquid films now transform into non-continuous isolated liquid droplets leading to reduced strength of the material at the weld line. In the very last stage, when fraction of solid exceeds 90%, the dendritic structure in the weld metal refines into a grain structure. A thin liquid film can still be present within grain boundaries due to the presence of segregated elements in the liquid, lowering the melting point of the film [26].

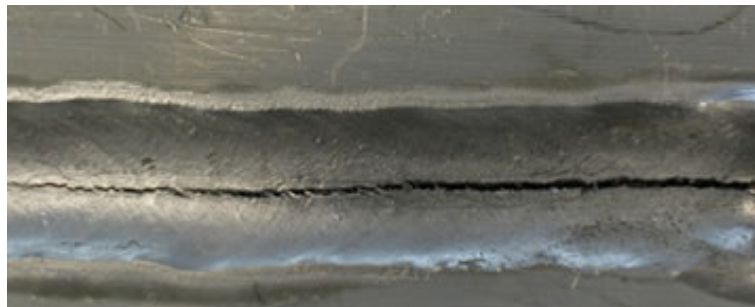


Figure 2.13: Hot crack in a welded joint [27].

These intergranular cracks appear in the surface of the center weld line, seen in Figure 2.14, but sometimes can also be seen in the HAZ known as liquation cracks.

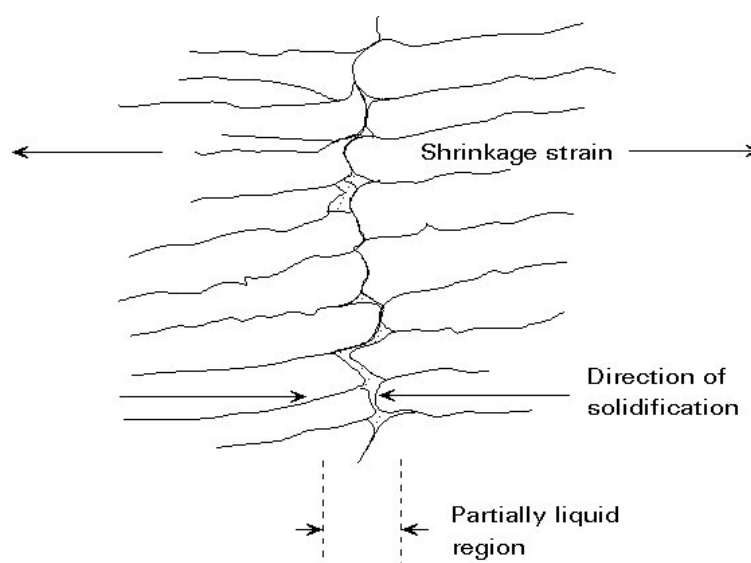


Figure 2.14: Schematic view of hot cracking [8].

It is a very complex phenomenon and it is difficult to figure out which of the factors have a more impactful contribution to cracking because they are all interacting simultaneously. Solidification cracks can usually occur due to a combination of:

- **Internal stresses** - factors such as material's mechanical properties and the welding conditions are responsible for producing these types of stresses;
- **External stresses** - given the mechanical clamping conditions for the weld to be performed.

In the literature, some relevant experiments were conducted with the CuCr1Zr alloy. Wisniewski *et al.* [25] evaluated how the thermophysical properties of a CuCr1Zr alloy would change when cooling down to room temperature in attempt to fully understand the solidification phenomenon in this specific alloy. Cylindrical samples were heated to 1200 °C with variable heat rate, then held isothermally at this temperature for 3 hours and, finally, steadily cooled down to room temperature. Figure 2.15 displays the curve of solidification of CuCr1Zr. The lowest temperature at which an alloy is completely liquid is  $T_L = 1080^\circ\text{C}$ .

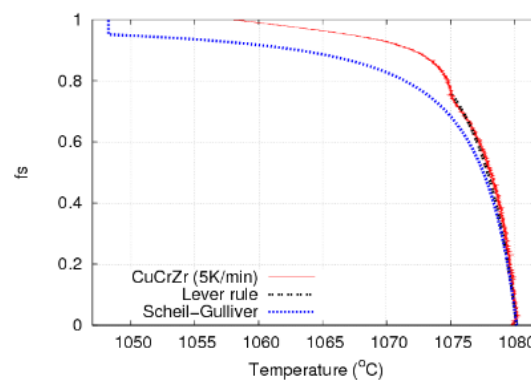


Figure 2.15: CuCr1Zr solidification curve. Solid fraction ( $f_s$ ) over temperature. [25]

This was an interesting study to understand how the material behaves under different working temperatures, be it during cooling or heating as thermal gradients are entirely related to the appearance of residual stresses. Wiesniwski *et al.* [25] concluded with this study that the thermal conductivity of CuCr1Zr was unusually higher in the liquid state.

Other conclusive studies were found to be effective in understanding the hot cracking phenomenon in CuCr1Zr, for instance, Durocher *et al.* [28] experimented with different batches of CuCrZr alloy to identify the EBW parameters which generated hot cracking. It was seen that higher welding speeds reduced the cracking, whereas deep focused beams into the work-piece would favour the appearance of cracks. Through various experiments, Durocher *et al.* [28] found that when optimal conditions were settled for the weld speed and focusing, non-propagating hot cracks were still present in overlapped zones due to remelting. Hot cracking was related to the seam geometry - depth of penetration and width. For deep and narrow seams, and thus relatively small HAZ, hot cracking did not occur.

## Chapter 3

# Finite Element Method (FEM)

Before FEM computer simulations of welding processes came into general use, the only way to present temperature fields during welding was through analytical methods. However, the emergence of modernized technologies, new materials, and the increasing complexity of the designed structures have made the operation of analytical methods highly difficult or even impossible in certain cases. **The development of packages for computer simulation of welding processes based on the FEM has opened up new possibilities in the field of design support for these processes.**

This chapter aims to provide a brief review on FEM based on the notes from the book [29] and the lecture notes from the course of computational mechanics [30]. A parallelism between Finite Element Analysis (FEA) involving mechanical loads and thermal loads was established based on a consultation of heat transfer reviewed textbooks such as *Lionhard* [31] and *Incropera* [32].

### 3.1 Tetrahedral Elements

The first step is to cover the geometry with suitable simple shapes. In this first section, one of the possibilities are solids with four triangular faces, the so-called tetrahedra. The covering must be performed without gaps or overlaps and such that two tetrahedra can share either a face, an edge, a vertex, or nothing (in the case where tetrahedra are not next to each other).

The motion within any single tetrahedron is entirely described by giving the displacements of the **so-called finite element nodes**, (the dots in Figure 3.1 indicate the locations of the finite element nodes), with the displacements of the material at any point within the element being determined from the displacements of the nodes using interpolation with very simple, polynomial, functions: the **so-called basis functions** which will be comprehensively explained later. So for the tetrahedron element exemplified below, the task of describing any deformation of this element boils down to giving the displacements of these exact ten points (nodes), and interpolating with known (given) functions of very simple form to obtain the displacement at an arbitrary point within the element. That is the essence of the FEM.

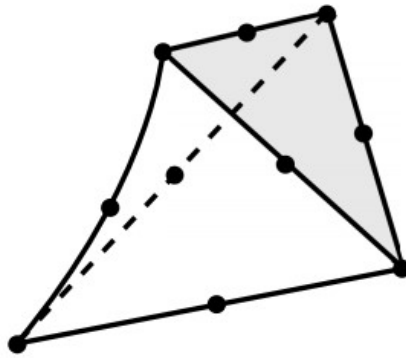


Figure 3.1: A single tetrahedral finite element.

These finite elements are also useful for a other tasks:

1. **Material properties** - for general use, the distribution of materials properties of a specific designed structure can be easily described;
2. **Easy computation** - the FEM relies on the ability to evaluate volume and surface integrals. Finite elements are perfect for this task since they have very simple shapes for which simple integration rules exist, and therefore easing computation for arbitrarily complex integrals.

## 3.2 Hexahedral Elements

The variety of finite elements available in the FEM softwares is due to the fact that some elements are better in one situation whilst the position can be reversed in a completely different situation. **There is no one size fits all** and so another type of finite element could be taken into consideration. Initially, a few things can be pointed out regarding hexahedral elements:

1. **Quality** - result quality is better using these types of finite elements and that is a general observation that can be made with respect to the relative merits of these elements;
2. **Accuracy** - the smaller the elements (meaning that more are in use), the more accurate the results become. **Accuracy is measured in terms of how close the finite element solution can get to the true solution.**

The process of getting closer to the true solution is called **convergence**, and without convergence there would be no point in using the FEM, because it wouldn't be possible to rely on the results being relevant to conducted researches.

### 3.3 Symmetry

Using symmetry can be a clever way to simplify calculations and facilitate convergence problems. The geometry and the heat-transfer conditions (the material, the load, the boundary conditions) possess two kinds of symmetry:

- **Axial Symmetry** - for instance, the axis of the cylinder is an axis of symmetry for this geometry;
- **Translational Symmetry** - the geometry moves in a specified direction. The solution is independent of the transverse coordinate or axis (e.g: Z-axis).

It is important to make use of symmetry to increase simulation efficiency.

### 3.4 Heat Transfer

Understanding the phenomena of heat transfer in solid structures is of considerable interest. The effects of the temperature that varies from point to point across the structure are twofold:

1. The change of the temperature from the reference value leads to the so-called thermal strains, which cause deformation and generate stresses;
2. The properties of the material may depend on temperature. As an example: the high temperature softening of metals. Therefore also the deformation and the stress in the structure will change as a result of the change of the properties of its material.

The mathematical model of heat conduction is both simple and important: and at the same time thermal loads on structures are the second most important kind of loads (after “mechanical” loads). The heat conduction model is described by the partial differential equation for the temperature  $T$ .

$$-\kappa \cdot \operatorname{div} \left[ \left( \operatorname{grad}(T) \right)^T \right] - q = 0 \quad (3.1)$$

It is expected to be satisfied at all points of the volume  $V$ . Here  $T$  is a function of the Cartesian coordinates  $x, y, z$  and represents the distribution of temperature across the volume of the part;  $q$  is the rate of heat generation in units of power per unit volume; and  $\kappa$  is the so-called thermal conductivity which is a property of the concrete material; the material is assumed to be the same everywhere within  $V$  (i.e. homogeneous). The  $\operatorname{div}$  and  $\operatorname{grad}$  are the divergence and gradient operators, respectively.

Explicitly it can be written:

$$-\left(\frac{\partial^2 T}{\partial x^2} + \frac{\partial^2 T}{\partial y^2} + \frac{\partial^2 T}{\partial z^2}\right) - q = 0 \quad (3.2)$$

This equation expresses the balance of heat energy, and if a solution is found, it will hold at every single point in the volume  $V$ . **The boundary conditions are the decisive part of the mathematical model:** they can make the solution unique, and they are crucial in deciding whether or not the solution exists in the first place. Physically the boundary conditions are an expression of the interaction of the world with a subset of it that is desired to model - in the present case, limiting to a simple three-dimensional body. The interaction of this modeled three-dimensional body with the environment in which it exists (other three-dimensional bodies, the ambient properties around, and so on) is expressed through the interactions that the modeled body has with the not-modeled rest of the world. **This interaction occurs across the boundaries.**

The main problem in finite elements method is to choose an adequate shape or integration function to provide approximate variation of the depended variable within each element between the values of the nodes. In this case, the temperature is assumed to vary linearly across each element. Consequently, it is possible to write the temperature variation within any element as:

$$T(x, y, z) = \alpha + \beta x + \gamma y + \delta z \quad (3.3)$$

These coefficients are particular to each and every element, but they aren't always independent. In fact, the **temperature needs to be continuous across the entire mesh** (as it is continuous in the analytical solution), so there must be some relationships between the sets of coefficient in one tetrahedron and its neighbors. This means that the temperature described on one tetrahedron must match that described on the other. It is possible to rewrite Equation 3.3 as follows:

$$T(x, y, z) = \sum_i T_i N_i(x, y, z) \quad (3.4)$$

Where  $T_i$  is the temperature degree of freedom  $i$  and  $N_i$  is the so-called **basis function** or **shape function**. It is a linear function of  $x, y, z$  and its main properties are that it is either zero or one at each of the nodes of the element. The Degrees of Freedom (DoF) are the values of the temperature at the nodes. Some DoF are fixed by the boundary conditions, others needs to be calculated from the finite element equations: these are free (as opposed to fixed).

Another important note to take is that the expressions for the basis functions can be also easily differentiated to obtain the gradient of temperature at any point, but it is well known that in computing whenever a derivative is taken, accuracy is reduced.

### 3.5 Finite Element Analysis (FEA)

The boundary conditions can be incorporated into the FEM. Rearranging Equation 3.2 in matrix form:

$$[K_{ije}] \cdot [T_{ij}] = [Q_{ij}] \quad (3.5)$$

Where  $K_{ije}$  represents the conductivity matrix,  $T_{ij}$  the nodal temperature and the  $Q_{ij}$  the thermal load. FEM yields discrete equations that are entirely local to the element and hence the global matrix  $[K_{ij}]$  is a simple combination (sum) of local matrices for each node. Solving the system of equations, **the unknown nodal temperature** can be received as a result.

### 3.6 Heat Source Model

Goldak *et al.* [1] proposed various basic heat source models that can be readily used for welding numerical simulations. Three different simple models are presented in Figure 3.2:

- **Point heat source** - most basic type of heat source which is typically used to model shallow welds. It is placed on the top surface of the welded object;
- **Line heat source** - this type of heat source models deep welds. It places a line source which is perpendicular to the top surface of the welded object;
- **Disk heat source** - similar to the point heat source, but assumes heat flux assigned on the top surface of the object represented by a disk. It considers uniform (Gaussian) distribution.

Gaussian distribution is described using the following function which corresponds to Figure 3.2a.

$$q(r) = q(0)e^{-Cr^2} \quad (3.6)$$

Where  $q(r)$  is the heat flux in function of the distance  $r$ ,  $q(0)$  is the nominal value for the heat flux at the center of the disk,  $C$  is a heat flux distribution constant and  $r$  is the distance from the disk center. Moreover, it is extended by a three-dimensional hemi-spherical heat source which is placed beneath the top of the surface of the welded object.

Disk heat source and hemi-spherical heat source assume that the geometry of the weld pool is completely symmetric with regards to the Z-axis. Thus, this model fails to represent a weld pool created by a moving heat source.

To solve this issue, **an ellipsoid weld pool was considered due to its oval shape**. Since temperature gradients in the front part of the weld pool are lower than in the rear part, another ellipsoid was used to accurately represent these temperature gradients. This is the **so-called double ellipsoid heat source model**. Heat flux distribution can be represented by the following equation corresponding to Figure 3.2b.

$$q(x, y, z, t) = \frac{6\sqrt{3}fQ}{abc\sqrt{\pi\pi}} e^{-\frac{3x^2}{a^2}} e^{-\frac{3y^2}{b^2}} e^{-\frac{3(z+\nu t)^2}{a^2}} \quad (3.7)$$

Where  $Q$  is the overall heat input,  $f$  the fraction of power assigned to the ellipsoid quarter,  $a, b, c$  being the ellipsoid semi-axis,  $\nu$  the heat source speed and  $t$  is the time that has passed since the beginning of the weld process.

Goldak *et al.* [1] stated that the previous model ended up being relatively accurate for description of heat distribution in shallow welds that are produced by electric arc welding process. For the purpose of heat distribution description in deep welds occurring during LBW and EBW, a conical heat source model can be employed. It assumes an Gaussian-like axisymmetric distribution. It is based on a heat distribution in radial direction and linear heat distribution in axial direction. Such model can be seen in Figure 3.2c [33].

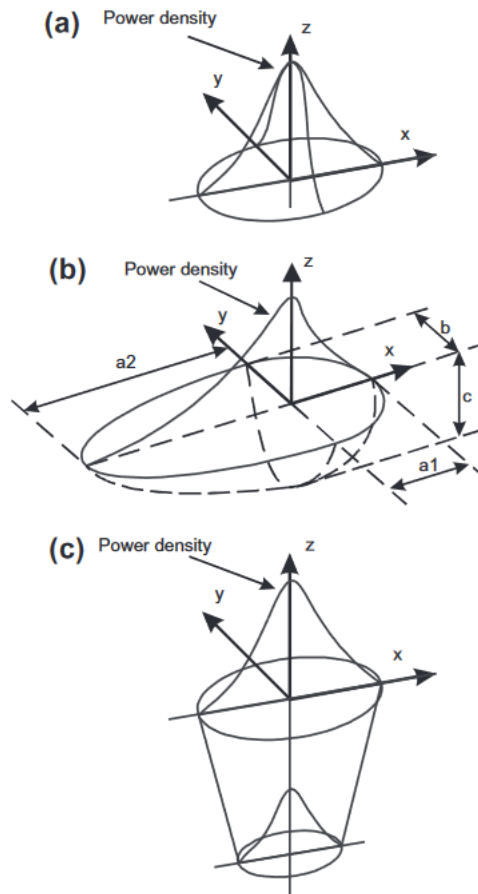


Figure 3.2: Heat source models: (a) disk source, (b) double ellipsoid source and (c) conical source [34].



The heat source model considers the power applied and also takes into account the gaussian parameter which measures how stiff the normal distribution is as well as the conical upper radius, conical lower radius, conical depth, the welding velocity and the process efficiency. Equation 3.8 and Equation 3.9 describe the heat source distribution.

$$q(x, y, z) = \frac{\eta P}{v} e^{-M \frac{x^2 + y^2}{r_0^2(z)}} \quad (3.8)$$

$$r_0(z) = r_e + \frac{r_i - r_e}{z_i - z_e} (z - z_e) \quad (3.9)$$

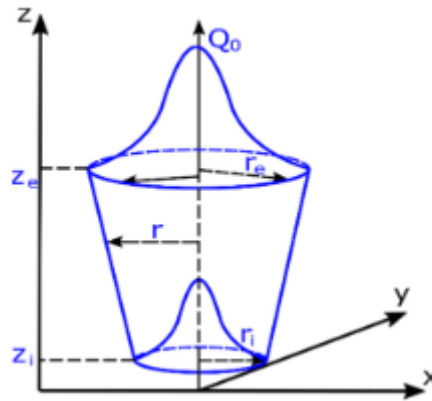


Figure 3.3: Detailed 3D conical heat source [35].

## Chapter 4

# Design of Experiments (DoE)

In this thesis, experimental and numerical results will be very restricted due to the availability of material's samples and to the long simulation times required on FEA, respectively. Therefore, a statistical analysis which balances out accuracy with reliability must be carried out. There are various process factors that can be changed, meaning countless combinations are possible. Thus, simulating every single combination is unrealistic and unattainable. Varying more than one parameters at a time, would give a better an understanding on which parameters are more impactful for EBW simulations.

This chapter should give some clear insight into the general domain of Linear Regression (LR) methods as well as into the most commonly used model assessment techniques. It is widely based on Técnico's lecture notes from Amado [36], Noble [37] and statistics books for engineers [38, 39].

### 4.1 Linear Regression (LR)

Regression aims to explain the relationship between a response variable  $y$  and one or several independent (or regressor) variables  $x$ . In the sense of LR it is thus sought to fit a straight line (linear) to the given data as best possible and thus a model of the following form is assumed in Equation 4.1:

$$y_i = \beta_0 + \sum_{j=1}^k \beta_j x_{ij} + \epsilon_i \quad \text{for } i = 1, \dots, n \quad (4.1)$$

Herein, the subscript  $i$  indicates the  $i$ th observation of the respective variable and  $n$  denotes the total number of observations, where  $n > p = k + 1$  must hold.  $\epsilon_i$  denotes the error or noise term in the respective  $i$ th observation. From the statistical point of view, this is an unobserved random variable with an expected mean of 0 and a variance of  $\sigma^2$ . **Furthermore, the error terms of each observation are to be independent of each other.**

LR corresponds to case of  $k = 1$  in previous Equation 4.1, whereas if  $k > 1$  it is the case of multiple LR. The term 'linear' indicates that the model is linear in the **so-called regression coefficients**  $\beta_j$ , not necessarily in the regressor variables  $x_j$  for which any functional form is permitted. Lastly, the term  $\beta_0$  is called the intercept term. Equivalently, the above model can be written in matrix notation, which is often more practical when doing more complex calculations.

$$y = X\beta + \epsilon \quad \text{with } \epsilon \stackrel{iid}{\sim} N(0, \sigma^2 I) \quad (4.2)$$

$$\text{where } y = \begin{pmatrix} y_1 \\ \vdots \\ y_n \end{pmatrix}, \quad X = \begin{pmatrix} 1 & x_{1,1} & \cdots & x_{1,k} \\ \vdots & \vdots & \ddots & \vdots \\ 1 & x_{n,1} & \cdots & x_{n,k} \end{pmatrix}, \quad \beta = \begin{pmatrix} \beta_0 \\ \beta_1 \\ \vdots \\ \beta_k \end{pmatrix}, \quad \epsilon = \begin{pmatrix} \epsilon_1 \\ \vdots \\ \epsilon_n \end{pmatrix} \quad (4.3)$$

In order **to have a meaningful model for the prediction of the response variable** for a given set of values for the regressor variables, the unknown **regression coefficient vector**  $\beta$  **needs to be estimated**.

## 4.2 Least Squares Method (LSM)

The LSM focus on minimizing the distance between a function and its sampled data points. It is often employed in regression analysis, particularly in nonlinear regression modeling in which a curve is fit into a set of data. The idea behind LSM is to determine the regression coefficients in such a way that the error (or residual) sum of squares is minimized.

$$S = \sum_{i=1}^n \epsilon_i^2 = \sum_{i=1}^n \left( y_i - \beta_0 - \sum_{j=1}^k \beta_j x_j \right)^2 \quad (4.4)$$

Using elementary matrix derivation, the optimal solution turns out to be the well-known least squares estimator.

$$\hat{\beta} = (X^T X)^{-1} X^T y \quad (4.5)$$

- $X^T X$  needs to be invertible for this estimator to exist. This can be guaranteed if the matrix  $X$  has full rank  $p = k + 1$  and it thus holds that  $|X^T X| \neq 0$ .

### 4.2.1 Properties of the Least Square Estimator

There are numerous good reasons why the least squares estimator is widely used for fitting LR models and overall in statistics.

- One of the most important properties of  $\hat{\beta}$  is that it is **unbiased**, i.e.  $E[\hat{\beta}] = \beta$ . This property can be extracted straightforwardly when keeping in mind that  $E[\epsilon] = 0$ . Moreover, the least squares estimator is even the best linear unbiased estimator;
- The covariance matrix of  $\hat{\beta}$  can be determined as  $Cov[\hat{\beta}] = E[(\hat{\beta} - E[\hat{\beta}])(\hat{\beta} - E[\hat{\beta}])^T]$  which turns out to be equal to  $\sigma^2(X^T X)^{-1}$ .  
This also means that  $Var[\hat{\beta}_j] = \sigma^2(X^T X)^{-1}_{jj}$  and  $Cov[\hat{\beta}_{j_1}, \hat{\beta}_{j_2}] = \sigma^2(X^T X)^{-1}_{j_1 j_2}$ .
- $\epsilon \stackrel{iid}{\sim} N(0, \sigma^2 I)$ , the least squares estimator also follows a normal distribution.

$$\hat{\beta} \sim N(\beta, \sigma^2(X^T X)^{-1}) \quad (4.6)$$

- For independent and normally distributed error terms, the least squares estimator can be shown to coincide with the maximum likelihood estimator.

### 4.2.2 Confidence Intervals for the Least Squares Estimator

In the statistical framework the ‘confidence interval’ represents an unreliability or uncertainty associated with each of the estimated parameters. Thus, it is usually intended to compute ‘intervals’ for evaluating accuracy of the estimator. The estimated response by means of the least square estimator is given:

$$\hat{y} = X\hat{\beta} \quad (4.7)$$

As an estimator for the error  $\epsilon$ , the **so-called residual** is achieved, which is defined to be the difference between the observed (actual) response vector and the fitted vector:

$$r = y - \hat{y} \quad (4.8)$$

Unlike  $\epsilon$ , which is an unobservable error vector,  $r$  is observable and can be used to estimate the error variance  $\sigma^2$  by means of the residual (or error) sum of squares:

$$SSE = \sum_{i=1}^n r_i^2 = r^T r = (y - X\hat{\beta})^T (y - X\hat{\beta}) = \dots = y^T y - \hat{\beta}^T X^T y \quad (4.9)$$

For a model with  $p = k + 1$  parameters (including the intercept term) to be estimated, the error sum of squares has  $n - (k + 1)$  DoF and has an expectation of:

$$E[SSE] = (n - (k + 1))\sigma^2 \quad (4.10)$$

An unbiased estimator for  $\sigma^2$  is thus given by the mean squared error, which is the average error sum of squares obtained by dividing the error sum of squares by its DoF:

$$\hat{\sigma}^2 = MSE = \frac{SSE}{n - (k + 1)} \quad (4.11)$$

Now, the covariance matrix of  $\hat{\beta}$  can be estimated by replacing  $\sigma$  with its estimator  $\hat{\sigma}$ , thus allowing an estimate of the variance of the least squares estimators as  $Var[\hat{\beta}_j] = (X^T X)^{-1}_{jj} \hat{\sigma}^2$ .

Finally, this gives the following  $(1 - \alpha)$ -confidence intervals for the regression coefficients:

$$\beta_j \in [\hat{\beta}_j \pm t_{n-(k+1), 1-\alpha/2} \cdot \sqrt{(X^T X)^{-1}_{jj} \hat{\sigma}^2}] \quad (4.12)$$

The constant  $t_{n-(k+1), 1-\alpha/2}$  hereby denotes the  $(1-\alpha/2)$ -quantile of Student's t-distribution with  $n - (k + 1)$  DoF.

- **Confidence Intervals for the Fitted Values**

The distribution for the fitted variables can also be obtained from the distribution of  $\hat{\beta}$ . This leads to the following  $(1 - \alpha)$ -confidence interval:

$$y_i \in [\hat{y}_i \pm t_{n-(k+1), 1-\alpha/2} \cdot \sqrt{x_i^T (X^T X)^{-1} x_i \hat{\sigma}^2}], \quad (4.13)$$

In this case,  $x_i$  denotes the vector  $(1, x_{i1}, \dots, x_{ik})^T$ , that is the  $i$ th column vector of  $X$ .

- **Prediction Intervals for a new Observation**

The point prediction for a new observation is simply given by:

$$\hat{y}_{new} = \hat{\beta} x_{new}, \quad (4.14)$$

Where  $x_{new}$  denotes the vector of regressor variables for the new observation. Understandably, the development of the respective prediction intervals has to be done carefully.

A prediction interval has to take into account the error from the fitted model as well as the error associated with the future observation. Therefore, a  $(1 - \alpha)$ -prediction interval (or confidence interval for a new observation) is given by the following:

$$y_{new} \in [\hat{y}_{new} \pm t_{n-(k+1), 1-\alpha/2} \cdot \sqrt{(1 + x_{new}^T (X^T X)^{-1} x_{new}) \hat{\sigma}^2}] \quad (4.15)$$

## 4.3 Analysis of Variance (ANOVA)

ANOVA is the statistical tool most commonly applied to the results of the experiments to determine the percentage contribution of each parameter against a stated level of confidence. It states that the total variation in a data set can be partitioned into two parts, the regression (corresponding to a regression model) and the residual (corresponding to the error thereof) fractions, respectively:

$$\underbrace{\sum_{i=1}^n (y_i - \bar{y})^2}_{\text{SST}} = \underbrace{\sum_{i=1}^n (\hat{y}_i - \bar{y})^2}_{\text{SSR}} + \underbrace{\sum_{i=1}^n (y_i - \hat{y}_i)^2}_{\text{SSE}} \quad (4.16)$$

Where SST denotes the total sum of squares, the squared deviation of each observation from the mean, SSR represents the part of the deviation that can be explained by the regression model and SSE expresses the part of the deviation associated with the residuals.

It needs to be addressed that the above sum of squares will usually increase with the number of observations, as they are unscaled measures. **For this reason, mean squares are often employed**, which are simply the sum of squares divided by their respective DoF.

Source	DoF	Sum of Squares	Mean Squares
Regression	$n - (k + 1)$	SSR	$M_{SSR} = \frac{SSR}{n - (k + 1)}$
Residual	k	SSE	$M_{SSE} = \frac{SSE}{k}$
Total	$n - 1$	SST	$M_{SST} = \frac{SST}{n - 1}$

A second important result states that the error sum of squares divided by the true error variance follows a  $\chi^2$  distribution with the same amount of DoF as the respective sum of squares.

$$\frac{SSE}{\sigma^2} \sim \chi_{n - (k + 1)}^2 \quad (4.17)$$

This now leads to a statistic test crucial to the model building process. A very clear example can be given, so considering the following two models:

$$\text{Model 1: } y_i = \beta_0 + \sum_{j=1}^k \beta_j x_{ij} + \epsilon_i \quad (4.18)$$

$$\text{Model 2: } y_i = \beta_0 + \sum_{j=1}^l \beta_j x_{ij} + \epsilon_i, \text{ for } l < k \quad (4.19)$$

It is of great interest to evaluate whether (any of) the additional regressor variables in model 1 are significant, that is whether model 2 is a good enough description of the process or not. More precisely, this can be formulated in the words of statistical hypothesis testing as follows:

$$\underbrace{H_0 : \beta_{k+1} = \dots = \beta_l}_{0\text{-hypothesis}} \text{ vs. } \underbrace{H_1 : \text{at least one of } \beta_{k+1}, \dots, \beta_l \text{ is non-zero}}_{\text{alternative hypothesis}} \quad (4.20)$$

Now, let  $SSE_1$  denote the error sum of squares for model 1 and  $SSE_2$  the error sum of squares for model 2 respectively. Since model 1 has more parameters than model 2 and thus  $SSR_1 \geq SSR_2$ , it holds that  $SSE_1 \leq SSE_2$  (since  $SST_1 = SST_2$ ). It is possible to rewrite  $SSE_2$  as follows:  $SSE_2 = SSE_1 + (SSE_2 - SSE_1)$ , where the second additive term is considered the excess sum of squares.

If the null-hypothesis holds, the following are true:

$$\frac{SSE_1}{\sigma^2} \sim \chi^2_{n-(k+1)}, \quad \frac{SSE_2}{\sigma^2} \sim \chi^2_{n-(l+1)} \quad \text{and} \quad \frac{SSE_2 - SSE_1}{\sigma^2} \sim \chi^2_{k-l} \quad (4.21)$$

Furthermore, under  $H_0$  it holds that  $SSE_1$  and  $SSE_2 - SSE_1$  are independent of each other. Putting these together, brings out the following F-statistic to test the hypotheses at hand. If  $H_0$  holds, then

$$F = \frac{(SSE_2 - SSE_1)/(k-l)}{SSE_1/(n-(k+1))} \sim F_{k-l, n-(k+1)} \quad (4.22)$$

$SSE_2$  large implies that at least one of the parameters  $\beta_{l+1}, \dots, \beta_k$  is non-zero and this significant. Therefore, one can reject  $H_0$  for large values of F. The general rule here is to reject  $H_0$  if  $F > F_{k-l, n-(k+1); \alpha}$  for a chosen **significance level**  $\alpha$ .

## 4.4 Model Selection and Evaluation

It is also important to choose a feasible model. There are several methods available that will help choosing an adequate model, especially if there are many possibilities available. Particularly when the number of influential variables is unclear, a stepwise selection might prove helpful. There are three different main approaches to such a selection process:

- **Forward Selection** - Here, the initial model consists of the constant intercept term only and other variables are included one by one if they prove statistically significant. That is, the most significant variable will be added first, others thereafter if they deliver a significant improvement to the new current model.
- **Backward Elimination** - Here, the initial model consists of all candidate variables considered test-worthy and variables are deleted one by one in case they turn out to be statistically insignificant. Again, the most insignificant term is removed from the model first.
- The most common stepwise regression method is a combination of the above and can either drop or add variables in each step.

There needs to be a means of assessing the quality of the models produced in each of the steps. The quality of the models can be verified using several possible existent criteria found in the literature [37, 40] and are as follows:

- **$R^2$ -value**

$$R^2 = 1 - \frac{\sum_{i=1}^n (Y_i - \hat{Y}_i)^2}{\sum_{i=1}^n (Y_i - \bar{Y})^2} = 1 - \frac{SSE}{SST} = \frac{SSR}{SST} = \frac{\sum_{i=1}^n (\hat{Y}_i - \bar{Y})^2}{\sum_{i=1}^n (Y_i - \bar{Y})^2} \quad (4.23)$$

Where  $\hat{Y}$  denotes the fitted value,  $\bar{Y}$  the average, SST the total sum of squares, SSE the residual (error) sum of squares and SSR the regression sum of squares.

It takes on values between 0 (no fit) and 1 (perfect fit) and corresponds to the square of Pearson's correlation coefficient in the case of simple regression and to square of the multiple correlation coefficient in the case of multiple regression.

This statistic shows the quality of the linear approximation, not however whether the model was specified correctly. Furthermore, it does not make an assertion about the statistical significance of the determined relationship. For this purpose, a special test needs to be conducted additionally. Last but not least, the  $R^2$ -value does not show whether or not a transformation of the data might give a better result, i.e. a more meaningful regression model.

Since the  $R^2$ -value of a model with additional regression variables is always greater than that for the initial model, no matter if the additional variables are in fact able to explain the regressor more precisely, an adjusted  $R^2$ -value that takes into account the number of regression variables in the model is usually applied to compare several models with each other. This value can be viewed in the following equation.

$$R_{adj}^2 = 1 - (1 - R^2) \frac{n-1}{n-p} \quad (4.24)$$

**In the regression output for Minitab 19 statistical software [41], the summary of the model provides both  $R^2$  and adjusted  $R^2$  values.** Besides it also provides the standard error of the regression S-value. It represents the average distance that the observed values fall from the regression line. Conveniently, it tells how wrong the regression model is on average using the units of the response variables. Smaller values are better because it indicates that the observations are closer to the fitted line.

- **AIC (Akaike's Information Criterion)** : This criterion can be used in the model selection process to **compare models with each other**, does not however give any information about how exceptional is the fit of either of them. It is formally defined as:

$$AIC = 2 \cdot p - 2 \cdot \log(L) \quad (4.25)$$

Where  $p$  represents the number of model parameters as usual, and  $\log(L)$  is the model's maximized log-likelihood function. As the aim is to find the model with **minimum AIC**, the first term in the definition is a penalty term to avoid over-fitting, i.e. including model parameters to increase the goodness of fit irrespective of the actual relationship between the regression variables and the regressor. For small (finite) data sets a correction is usually applied which uses a stronger penalty for additional parameters. This is given as:

$$AIC_{corrected} = AIC + \frac{2 \cdot p(p+1)}{n-p-1} \quad (4.26)$$



In the literature it was found that it was advised to use the  $AIC_{corrected}$  instead of the standard AIC regardless of dimension of the data sets, unless  $n$  is many times larger than  $p^2$  to avoid over-fitting.

- **BIC** (Bayesian Information Criterion): It is partially based on the likelihood function as it is sought to increase the likelihood of the estimation by adding parameters. As this may lead to over-fitting of the data, a penalty term concerning the numbers of parameters in the model is included.

$$BIC = p \cdot \log(n) - 2 \cdot \log(L) \quad (4.27)$$

This criterion is closely related to the AIC but penalizes the use of too many regression variables more vigorously.

## 4.5 Classical Designs

Before going into more detail about the advantages and disadvantages of, as well as the general settings in which optimal designs, mostly computer-generated designs, are to be employed, it is wished to review briefly the most commonly used standard designs and their most prominent characteristics [42, 43]. These designs are constructed to take on a certain (geometrical) form and as a natural consequence have special properties. **The proper choice of experimental design depends crucially on the experimental region to be investigated and on the model used to fit the response surface** [44] and can vary largely on the field of study [45]. Usually, the first step is to transform the natural data, which is given in some counting unit, into coded variables. Hereby, the coded values are chosen such that they are in the interval  $[-1, 1]$ . Assuming that the region of exploration for a factor  $\xi$  is given by  $[a, b]$ , this transformation can be achieved by applying Equation 4.28.

$$x = \frac{\xi - (a + b)/2}{(b - a)/2} \quad (4.28)$$

In the following subsections, since this field is vast, only a brief summary on these topics will be given, but merely focused on the designs that are of particular interest to this specific problem.

### 4.5.1 Full Factorial Design (FFD)

One of the most important design families are the FFD. Such designs contain all possible combinations of the factors' levels. Considering an example with three factors A, B and C and assume that each of these factors should be tested for  $a$ ,  $b$  and  $c$  different levels, then the resulting FFD will consist of  $a \cdot b \cdot c$  experimental runs. It should be clear that too many different levels will make the design size impractical, for which reason  $2^k$  or  $3^k$  designs are most commonly used. Here, a  $2^k$  denotes a design with  $k$  factors at two levels each and a  $3^k$  follows the same principle. Note that  $2^k$  or  $3^k$  respectively refers to the resulting number of experimental runs of such designs. Again, for  $k \geq 5$  factors this requires a number of experiments that might already be too large for many applications, even at only two levels.

Their importance arises mainly from the fact that they:

- Require relatively few runs per investigated factor;
- Can be upgraded to form composite designs, which are used in optimization;
- Form the basis for two-level fractional factorial designs, which are of great practical value at an early stage.

### 4.5.2 Fractional Factorial Design

In certain cases, it can be very time-consuming to get collect all the required data to build a FFD. In order to reduce the number of required experimental runs fractions of FFD are often used. If all factors are set at two levels a  $2^r$  fraction of a full  $2^k$  factorial design is denoted by  $2^{kr}$ . The choice of the fraction needs to be considered carefully since a fractional design does not allow to estimate all factors and interactions separately.

### 4.5.3 Central Composite Design (CCD)

The CCD is also a very useful tool in response surface methodology to fit a quadratic model. It is suggested to use for for spherical or cuboidal design regions.

$$y = \beta_0 + \sum_{i=1}^k \beta_i x_i + \sum_{i=1}^k \beta_{ii} x_i^2 + \sum_{i=1}^k \sum_{j < i} \beta_{ij} x_i x_j + \epsilon \quad (4.29)$$

#### • Brief summary

For this framework, the basics of linear and non-linear regression were explained as well as ANOVA. It was seen in **Minitab 19** that defining a confidence interval and the appropriate significance level  $\alpha$  was decisive and could definitely turn a rudimentary model into a better one using the methodology in Section 4.4 - by either dropping or adding interactions depending on their implication. For model evaluation, it was seen that **Minitab 19** directly gave statistical parameters S,  $R^2$ , adjusted  $R^2$  and predicted  $R^2$ . FFD was the chosen design since there were enough data-samples gathered from thermomechanical simulations. In case it was not possible to build a FFD, a fractional FFD or CCD would have been the preferred alternatives.

## Chapter 5

# Support Vector Machine (SVM)

Another statistical approach is by using machine learning algorithms that are capable of learning from experiences. There are two categories of learning: supervised methods, in which the learning has to find a function on basis of past experiences (and their labels in the case of classification), and the unsupervised methods, where the training does not need any examples. In the context of this thesis, a supervised machine learning algorithm: Support Vector Machine (SVM) will be selected for a binary classification problem.

SVM finds an optimal hyperplane that maximizes the margin between classes by using a small number of training samples known as support vectors [46]. SVM has a property of simultaneously minimizing the empirical classification error and maximizing the geometric margin [47].

SVM uses kernel method to perform regression and classification by transforming the data to the higher dimensional space by nonlinear transformation techniques. It separates the two classes by finding a linear spacing between them. This linear spacing is achieved, as the data is transformed into the higher dimensions it tends to spread the data out which makes a way to find the linear spacing between the classes to get separated [48]. Thus, the hyperplane is the greatest margin between the two classes. Figure 5.1 shows the concept of a hyperplane. Bold line shows the acceptable hyperplane which separates the data.

SVM is a supervised machine learning algorithm where it is given a set of inputs with the corresponding labels. The inputs are in the form of attribute vectors. SVM constructs a hyperplane that separates two classes to achieve maximum separation between the classes. By separating the classes with a large margin, generalization error is minimized. The objective of achieving the minimum generalization error is to predict the correct class of the data without any error or minimal error, when it arrives for classification [49].

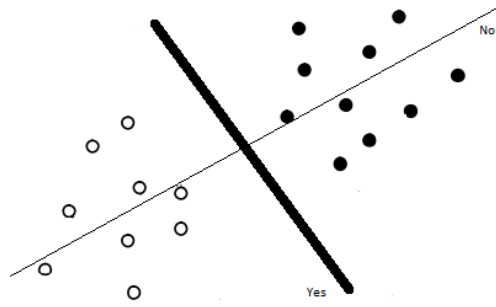


Figure 5.1: SVM Hyperplanes between two classes.

The two planes parallel to the classifier and which passes through one or more points in the data are called **bounding planes**. The distance between these bounding planes is called **margin**. By the process of learning hyperplane, which maximizes this margin, is evaluated. The points of the corresponding class, which falls on the bounding planes, are called **support vectors**. These points are crucial in forming a hyperplane hence the name support vector machine [49]. Figure 5.2 shows the concept of support vectors, bounding planes and maximum margin.

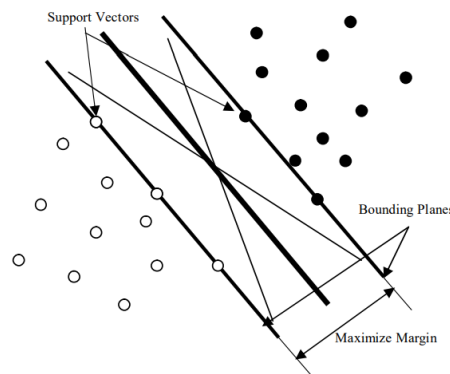


Figure 5.2: Bounding planes, support vectors and maximum Margin in SVM [49].

If the optimal hyperplane separates the training vectors without any errors, the ratio of the expectation of the support vectors to the number of training vectors limits the expected error rate. A good generalization is guaranteed if a small set of support vectors is found because this ratio is independent of the dimension of the problem [46]. In spite of taking all the required measures for classification, there are chances likely for misclassifications. SVM takes care of them, by allowing misclassifications of pixels between classes. Figure 5.3 shows two classes for classification, class A with white dots and class B with black dots. The hyperplane gives its maximum efforts in all the possible ways to classify the image with very less misclassification. The hyperplane is a straight line in this classification. It would be much more interesting if the hyperplane is a twisted line such that it surpasses the pixels of other class and classify the distinct classes without misclassification errors. Such type of classification with twisted separating boundary is known as nonlinear SVM classification.

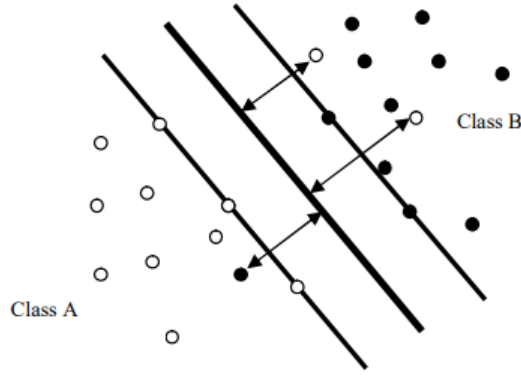


Figure 5.3: Misclassification in SVM [49].

SVM can be categorized into two distinct types:

- **Linear SVM** - if the hyperplane in the SVM classification has linear separation;
- **Nonlinear SVM** - if the hyperplane in the SVM classification consists of a nonlinear separation (achieved by using a kernel trick - functions that take low dimensional input space and transform it into a higher-dimensional space i.e. it converts not separable problem to separable problem.)

## 5.1 Linear SVM

If the hyperplane of the SVM is linear then such SVM is known as linear SVM. Linear SVM is applicable for two types of data. They are separable and non-separable type of data:

- **For Separable Data**

Considering  $n$  training pairs  $(y_i, x_i)$  where  $i = 1, 2, \dots, n$  having class labels  $y_i \in \{1, -1\}$  and  $x_i \in \mathbb{R}^2$ . If we consider the previous Figure 5.3 that displays two different classes A and B. In these equations class A is represented as +1 and class B as -1. The main goal of the SVM classifier is to introduce the aforementioned hyperplane, which separates all the points belonging to the A on one of the sides and B on the other. The hyperplane is defined as the plane separating the classes such that the closest vector in the two classes are farthest from the plane separating them as shown in Figure 5.3. It is noted by the following equation:

$$W \cdot x + b = 0 \quad (5.1)$$

Where,  $x$  is a point on the hyperplane and  $b$  is the distance of the closest point on the hyperplane to origin and  $W$  is a two dimensional vector pointing perpendicular to the hyperplane.

Let  $d_i$  be the perpendicular distance of vector  $x_i$  from any point  $x$  on the hyperplane. It is given by the equation:

$$d_i = y_i \frac{w}{|w|} \cdot (x_i - x) \quad (5.2)$$

This is further simplified by placing the hyperplane equation and the distance  $d_i$  as in equation:

$$d_i = y_i \frac{w \cdot x_i + b}{|w|} \quad (5.3)$$

The distance of the hyperplane from all the vectors must be minimum and the distances over the entire hyperplane placement must be maximum. Hence, the classifier becomes:

$$\max_{w,b} \min_{i=1,\dots,n} \left[ y_i \frac{w \cdot x_i + b}{|w|} \right] \quad (5.4)$$

It can be divided into two cases:

$$\begin{cases} y_i(w \cdot x_i + b) - 1 = 0 & \text{If } i \text{ is the nearest support vector to the hyperplane} \\ y_i(w \cdot x_i + b) - 1 \geq 0 & \text{If } i \text{ is not a support vector. } i = 1, \dots, n \end{cases} \quad (5.5)$$

The equation is further simplified and the optimal hyperplane for separable data is given by:

$$\min_{w,b} \frac{1}{2} |w|^2 \quad (5.6)$$

The optimization problem is solved by Lagrangian variables, where  $\lambda_i \geq 0$  and  $i = 1, 2, \dots, n$  are Lagrangian multipliers.

$$\mathcal{L}(w, b, \lambda_1, \dots, \lambda_n) = \frac{|w|^2}{2} - \sum_{i=1}^n \lambda_i [y_i(w \cdot x_i + b) - 1] \quad (5.7)$$

Subsequently:

$$\begin{cases} \max_{\lambda_1, \dots, \lambda_n} \min_{w,b} \mathcal{L}(w, b, \lambda_1, \dots, \lambda_n) \\ \lambda_i \geq 0 \text{ and } i = 1, 2, \dots, n \\ y_i(w \cdot x_i + b) - 1 \geq 0 \text{ where } i = 1, 2, \dots, n \end{cases} \quad (5.8)$$

The  $\lambda_n$  value must be maximized because by putting the Lagrangian multipliers minimum, the Lagrangian undetermined constraints reach the equality. Thus:

$$\lambda_i [(w \cdot x_i) + b] = 0 \text{ where } i = 1, 2, \dots, n \quad (5.9)$$

Equation 5.9 is known as complimentary condition. This can be further minimized by differentiating the function with  $w$  and  $b$  and we have the conditions as:

$$\frac{\partial \mathcal{L}}{\partial b} = 0 \text{ and } \frac{\partial \mathcal{L}}{\partial w} = 0 \quad (5.10)$$

The conditions stated in previous equations are known as Karush – Kuhn – Tucker optimality conditions.

- **For Non-Separable Data**

SVM classifier for non-separable data is a relaxed version of the separable data known as soft margin classifier [48]. A new variable known as slack variable ( $\zeta_i$ ) is introduced which allows a certain amount of misclassification. Where  $\zeta_i \geq 0$  and  $i = 1, 2, \dots, n$ . Hence, the equation of the hyperplane with the slack variable can be written as:

$$y_i(w \cdot x_i + b) - 1 + \zeta_i \geq 0 \text{ where } i = 1, 2, \dots, n \quad (5.11)$$

The equation of the optimal hyperplane is derived by solving the equation:

$$\min_{w, b, \zeta_1, \dots, \zeta_n} \left[ \frac{1}{2} |w|^2 + C \sum_{i=1}^n \zeta_i \right] \quad (5.12)$$

Where, C is a regularization constant which minimizes the solution for which  $\zeta_i$  get larger. Hence, C is an important parameter, which decides the appropriate hyperplane of the classifier. The only difference between the separable and non-separable dual problems is that in non-separable data the Lagrangian dual variables are bounded by the constant C making an impression that the non-separable data is valid only when  $\zeta_i = 0$ . The classifier becomes soft when  $\zeta_i > 0$ . The points, which are non-separable, are calculated and segregated by applying the condition  $\lambda_i = C$ .

## 5.2 Nonlinear SVM

Not always non-separable data have a solution using linear SVM classifier. There exist certain cases where linear classifier fails to find an optimal solution of classification. In such situations, nonlinear type of classification is used. The decision surface is nonlinear in this type of classification unlike linear in the linear type of classification. A nonlinear hyperplane is achieved by introducing a nonlinear kernel to perform a non-linearity transformation of the input data  $x_1, \dots, x_n \in X$  into a high-dimensional feature space using a map  $\phi : x_i \mapsto \phi(x_i)$  and then creating a linear separation in the newly defined space. Mathematically:

$$\langle \phi(x_i), \phi(x_j) \rangle = k(x_i, x_j) \quad (5.13)$$

where k is a positive definite kernel. The kernel trick states that, given an algorithm which is formulated in terms of a positive definite kernel k, one can construct an alternative algorithm by replacing k by another positive definite kernel k'; the dot product is a linear positive definite kernel and hence we can apply the kernel trick. Some of the most used positive definite nonlinear kernels are:

- **Polynomial**

$$k(x, x') = \langle (x, x') \rangle^d \quad (5.14)$$

where  $d \in \mathbb{N}$ . The polynomial kernel of degree d computes a dot product in the space spanned by all monomials of degree d in the input coordinates.

- **Inhomogeneous Polynomial**

$$k(x, x') = (\langle (x, x') \rangle + c)^d \quad (5.15)$$

similar to the polynomial kernel where  $d \in \mathbb{N}$  and  $c \geq 0$

- **Radial Basis Function (RBF)**

$$k(x, x') = \exp(-\sigma \|x - x'\|^2) \quad (5.16)$$

or

$$k(x, x') = \exp\left(-\frac{\sigma \|x - x'\|^2}{2\sigma^2}\right) \quad (5.17)$$

where  $\sigma > 0$  and it is the variance and the hyperparameter. The maximum value of the RBF kernel is 1 when  $x = x'$ , which means the distance between the two points  $X_1$  and  $X_2$  is 0 (meaning extremely similar). If the two points are separated by a large distance (meaning – not similar), then the value will be much less than 1 or close to 0.

- **Sigmoid Function**

$$k(x, x') = \tanh(\alpha x^T x' + C) \quad (5.18)$$

The Sigmoid Kernel comes from the Neural Networks field, where the bipolar sigmoid function is often used as an activation function for artificial neurons. There are two adjustable parameters in this kernel, Slope –  $\alpha$  and constant  $C$  – intercept.

## 5.3 Tuning Parameters

Some parameters included in the optimization problems are not known a priori and are not estimable through the SVM optimization process. Therefore, these parameters need to be tuned, i.e., go through a different estimation procedure. When using SVM with a linear kernel, there is only one parameter to be tuned: the misclassification parameter  $C$ . When using a RBF kernel other parameters need to be tuned increasing the complexity of the SVM model. The best value for tuning a parameter for a given problem is unknown but the criteria to choose it is based on the prediction accuracy for any new observation.



## Chapter 6

# Proposed Method

A proposed solution for minimizing tensile stresses during solidification was explored based on the available solutions in regards to this framework. For instance, one possible solution to minimize welding residual stresses actively was using the Low Stress No Distortion technique (LSND).

### 6.1 Low Stress No Distortion (LSND)

LSND employs auxiliary cooling or heating sources to manipulate thermal gradients, generating a specific temperature field altering the stresses occurring in the weld zone. The effects on the stress magnitude using LSND can be seen in Figure 6.1.

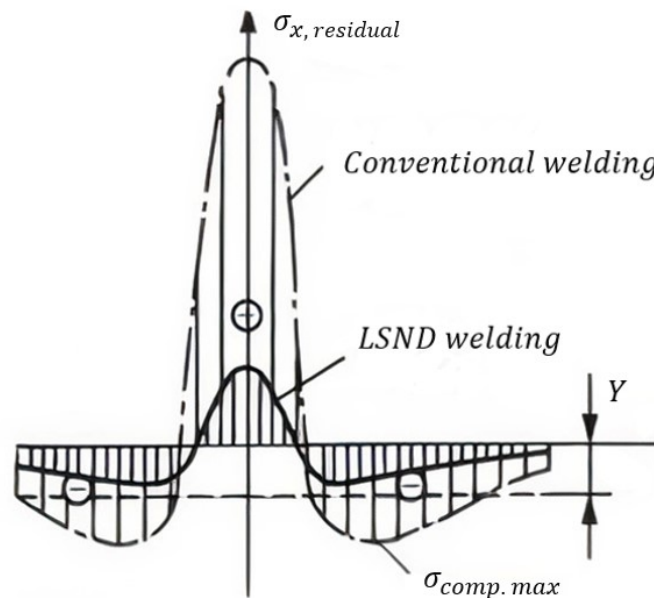


Figure 6.1: Residual stresses comparison [3].

An innovative technique picked up on the concept of LSND used an heat sink behind the heat source instead of having heating elements. The heat sink of this Dynamically-Controlled LSND method (DC-LSND) benefited from cooling elements such as  $CO_2$  snow which **drastically reduced temperature at the weld area** allowing for modification of temperature distribution in order to reduce residual stresses and distortion.

Although, theoretically this would prove to be effective, it was investigated that this cooling by  $CO_2$  caused hardening and brittleness of the weld metal [4]. Later, a modified DC-LSND that applied double cooling nozzles at both sides of the weld zone was examined. It increased hardness and strength of the weld metal, refining the micro structure. Modified DC-LSND displayed the same fatigue crack growth rate, but did not show any signs of embrittlement of the weld metal. Allowed reduction of distortion up to 95%, as opposed to just 81% on standard DC-LSND.

## 6.2 Multi Beam Technique

The previous method and its variations are often either time-consuming and may also change the micro structures alongside with mechanical properties [50]. A prosperous solution proposed a main welding beam while simultaneously applying multi-beam preheating on the side of the weld is shown in Figure 6.2, [51, 52]. Zhang *et al.* [51] found that the main advantages of this process over others, were that other processes needed to employ complicated, heavy and costly additional facilities to generate heating or cooling sources, while this method used electromagnetic deflection to generate both welding and pre-heating beams, so there was no need to use auxiliary heating or cooling devices. Another advantage was the fact that due to EBW characteristics, pre-heating beams could be generated as small as needed, making it possible to produce localized pre-heating areas with any geometric shapes and sizes.

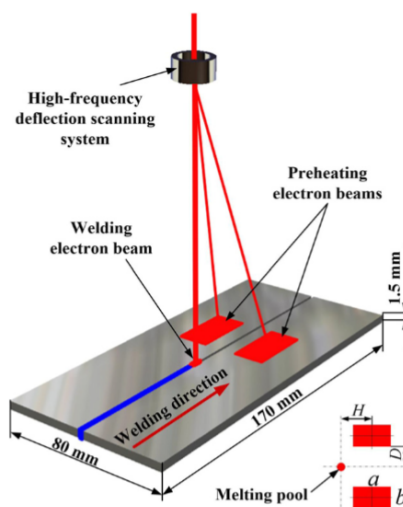


Figure 6.2: EBW with multi-beam preheating [51].

### 6.3 Thermally Induced Reduction of the Load (TIRL)

Based on the existent approaches seen in Section 6.1 and Section 6.2 a distinctive procedure is presented and investigated in this thesis. In this procedure, a thermal induced reduction of the load was applied through an additional beam - Secondary Heat Source (SHS). It is known that thermal loads induce changes in the mechanical fields and rapid heating and cooling rates can introduce tensile or compressive stresses - depending on the position between both Main Heat Source (MHS) and SHS. The idea was to ensure that this SHS, **only** introduced compressive stresses during the solidification of the weld pool through a local treatment, while the MHS associated with the welding process caused melting. An illustration is presented in Figure 6.3.

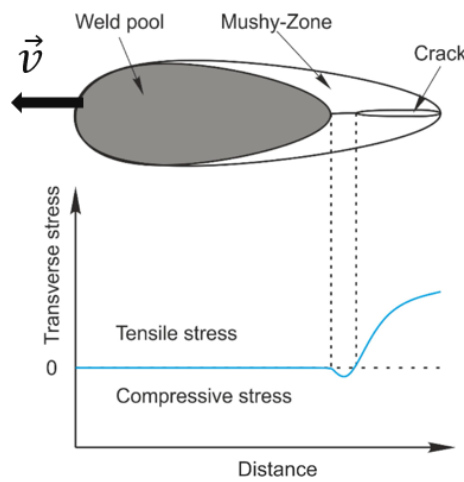


Figure 6.3: Illustration of the TIRL mechanism [53].

As explained previously in Section 2.6, hot cracking occurs in the latest stages of solidification. The blue line represented in previous Figure 6.3 represents the magnitude of the stresses, by introducing compressive stresses using a SHS, it was possible to lower the total magnitude of the tensile stresses. It was of utmost importance to come up with a proper methodology to make sure that the SHS was, in fact, introducing compressive stresses. A visual representation of how this solution theoretically works is presented in Figure 6.4.

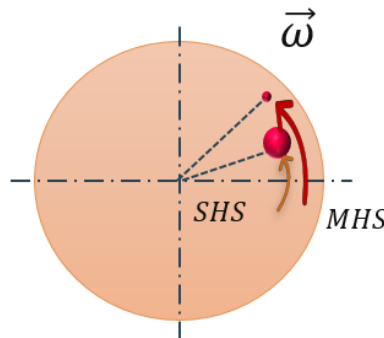


Figure 6.4: Sketched top view representing the TIRL mechanism.

Visually, that is a representation on how the TIRL should work. It was also important to define a criteria that separated the case of hot cracking from its absence. The criteria proposed is shown in Equation 6.1.

$$\sigma_{tensile} < \sigma_{proof} \quad (6.1)$$

In the present case, if the total magnitude of the **tensile stresses** during the latest stages of solidification of the weld pool was lower than the **admitted proof stress (or yield stress)** of the material CuCr1Zr, then theoretically it would be possible to avert the occurrence of hot cracking.

## 6.4 Methodology

To implement the TIRL method, thoroughly explained in Subsection 6.3 it was critical to define an adequate methodology. For this, the one factor at a time (OFAT) method was used to give a general feel on how the variables affected the outcome. It was necessary to establish which were the variables (or process parameters) that were suspected to be most impactful on the results. Conclusively, the statistical tool DoE was used for parameter configuration optimization.

### 6.4.1 Secondary Heat Source (SHS)

The essential parameters that were considered for the SHS: the angle, radial distance, power and representative dimension of the SHS are summarized in Figure 6.5.

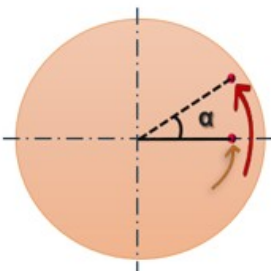
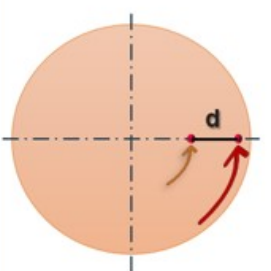
Angle between MHS and SHS (°) $\alpha$	Radial distance between MHS and SHS (mm) $d$	Power of SHS $P$	Representative dimension of SHS: $D_{SHS}$ (mm) $D$
		$P_{MHS}^* = 2.8 \text{ kW}$ $P_{SHS} = \% \text{ of } P_{MHS}$  $* P_{MHS}$ is the power of the main heat source	$D = 0.075 \text{ mm}^{**}$  $**$ This is an arbitrary initial value

Figure 6.5: SHS parameters.

These were considered to be the most influential parameters as they, in the end, would allow to construct a feasible DoE. Choosing too many variables would lead to impractical DoE models (as stated in Subsection 4.5.1).

The position between both heat sources was considered relevant - the angle and the radial distance. The power applied by the SHS was ensured as to only cause a local treatment, not allowing any melting. Since the process itself allowed to reproduce a secondary beam with variable size, the dimension of the SHS was also considered, combined with the power leading to the power density of the SHS.

### 6.4.2 One Factor at a Time (OFAT)

An OFAT procedure was applied to establish the value ranges for the aforementioned parameters in Subsection 6.4.1. A schematic representation of the methodology applied for the OFAT approach is presented in Figure 6.6. This is a simplified flowchart.

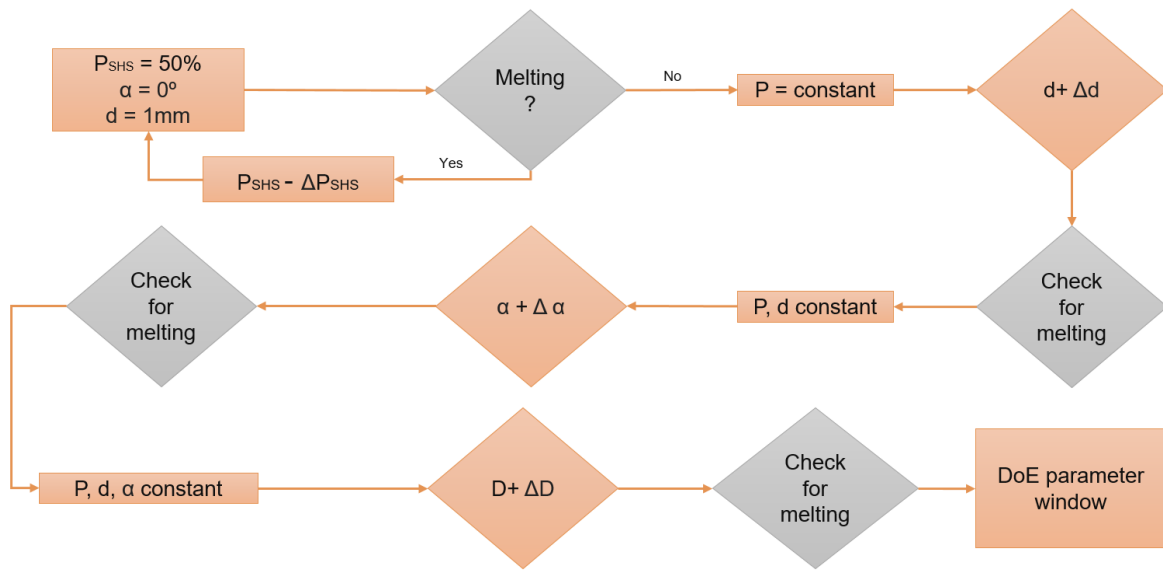


Figure 6.6: Flowchart depicting the methodology implemented to define the working range of process parameters.

Initially, a very generic extreme condition was considered. Both heat sources were placed side by side ( $\alpha = 0^\circ$  and  $d = 1\text{mm}$ ) and a  $P_{SHS} = 50\%$ . The arbitrary value for the diameter was chosen as the one displayed in Figure 6.5. It was necessary to check if SHS caused melting on the workpiece **at every iteration**. If that was the case, then the respective parameter was carefully and slowly adjusted to make sure this would not happen. In the case of no melting caused by the SHS, the parameter was set as a constant value and it was possible to move onto the next one (parameter). **This was performed successively for all influential variables**. Based on this factor examination, a systematic experimental approach using DoE was employed to assess statistical significance of the parameters and yield an optimum solution that avoided solidification cracking.



## 6.5 Numerical Implementation

This section describes the development of the finite element models used. First, the geometric modelling is described, followed by the finite element modelling. SolidWorks was the chosen for Computer-Aided Design (CAD) software and Simufact Welding as the FEM software.

Simufact Welding is designed for modeling and simulation of a wide range of thermal joining processes. Additionally, it also provides possibilities to model heat treatment processes, variations of cooling and unclamping setups as well as mechanical loading of welded structures making it suitable for these types of thermal and thermomechanical simulations.

It was necessary to define the geometry (domain discretization and boundary conditions), material properties and the heat source model as accurate as possible to reproduce the best results whilst allowing efficient computation. Numerical implementation methodology widely based on the referenced articles seen in [54–56].

### 6.5.1 Geometry Discretization

The geometry achieved in SolidWorks was a simple revolving geometry, with a small void inside. **The detailed geometry measurements were omitted from this thesis due to confidentiality reasons.** The hollow cylinder was clamped at the bottom, so all the movement and the moments in every axis were constrained. The first geometry model built used activating elements which in theory would produce the most accurate results, but the results regarding the thermal distribution throughout the surface showed various inconsistencies between elements.



Figure 6.7: Hollow cylinder geometry.

The final model comprised of 4 components and a total of 97794 elements after exhaustively exploring alternatives to optimize simulation time such as: dividing the geometry in small components assembled together. It can be seen in the transverse cut-view representation in Figure 6.8 that the **(P1) component** where the heat source passed had a more refined mesh whereas further away from the heat source, the mesh was less refined (coarse) - this reduced the total number of elements. Decreasing the number of elements of the mesh also decreased the simulation time.

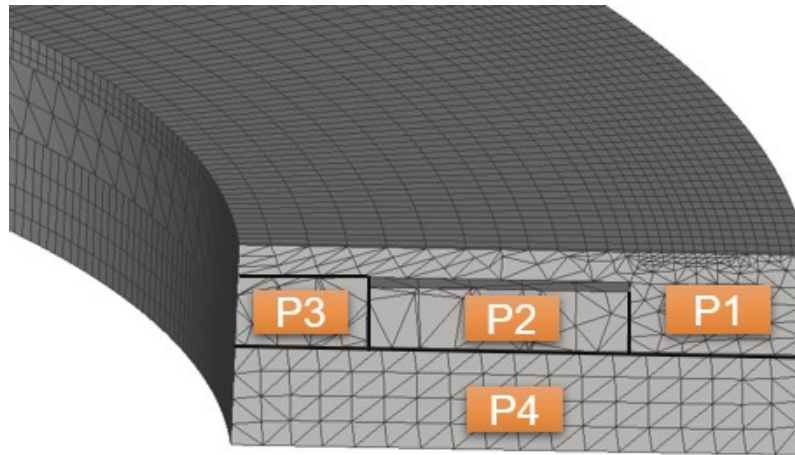


Figure 6.8: Transverse cut of the geometry.

Furthermore, for components P1 and P4 hexahedral elements were chosen for their improved quality over tetrahedral elements. Tetrahedral elements were chosen for P2 and P3 due to their simple shapes, therefore easing computation for arbitrarily complex volume and surface integrals in FEM. A clearer distinction between these types of elements is expressed in Section 3.1 and Section 3.2. Domain discretization details is evidenced in Table 6.1.

<b>P1 – 54492 Elements</b>	
Axial Dimension	1mm
Radial Dimension	2mm
Tangential Dimension	1mm
<b>P2 – 4797 Elements</b>	
Element Size	2.5mm
<b>P3 – 4089 Elements</b>	
Element Size	2mm
<b>P4 – 34416 Elements</b>	
Axial Dimension	3mm
Radial Dimension	3mm
Tangential Dimension	1mm

Table 6.1: Domain discretization.

For simulation purposes, the recursive solver, particularly the iterative sparse was used given that it improved simulation time - using direct methods with gaussian elimination was not needed for all the elements because the global stiffness matrix for the whole body had multiple locally sparse stiffness matrices wasting computing resources.



### 6.5.2 Material Properties

A similar alternative to the CuCr1Zr alloy was used since the exact properties of this alloy are not readily available in Simufact Welding material library. Material's thermophysical and mechanical properties are described in Table 6.2 and are at room temperature.

Thermophysical Properties	CuCr1Zr	Cu_SW
Density [g/cm <sup>3</sup> ]	8.89	8.86
Melting Temperature [°C]	1076	1084
Thermal Conductivity [W/(m.K)]	170	182
Specific Heat Capacity [J/(kg.K)]	380	414
Mechanical Properties	CuCr1Zr	Cu_SW
Tensile Stress [MPa]	380	380
Yield Stress [MPa]	300	300
Hardness Brinell [HB]	130	N/A
Young Modulus [GPa]	128	129

Table 6.2: CuCr1Zr vs. Cu\_SW properties at 20°C.

All values given in the software were empirically acquired for different temperatures, aside from the Poisson ratio which was considered constant over the whole temperature range. The flow curves relating the effective plastic strain with the flow stress for small strain rates were also attained through empirical experiences and are presented in Figure 6.9. There was no constitutive model found for this material in Simufact.

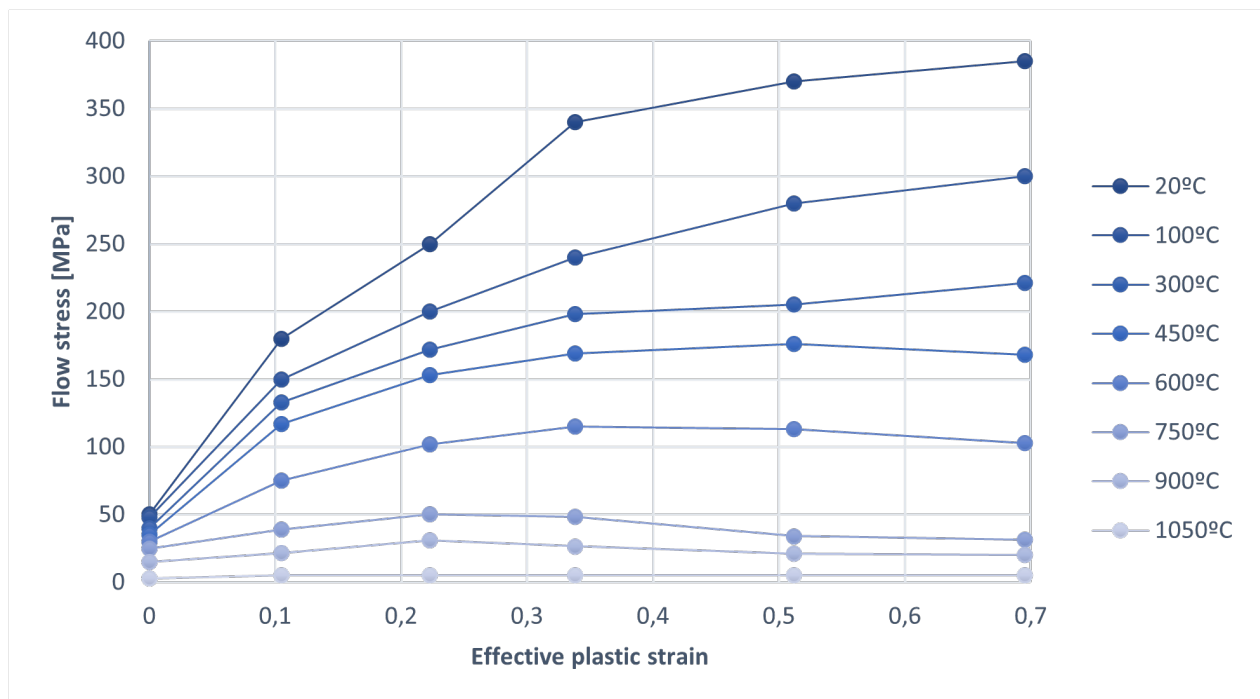


Figure 6.9: Flow curves for Cu\_SW.

For the criteria proposed in the methodology explained in Section 6.3, Equation 6.1 - the corresponding proof stress needed to be obtained using the flow curves. The values for the proof stress can be seen in Table 6.3 and are temperature dependent. **All other values not displayed in this table were linearly interpolated.**

<b>Temperature [°C]</b>	20	100	300	450	600	750	900	1050
<b>Proof Stress [MPa]</b>	250	200	160	140	110	40	25	5

Table 6.3: Temperature dependent proof stress of Cu.SW.

### 6.5.3 Heat Source Model

The Simufact Welding software uses the heat source models exposed in Section 3.6. For heat distribution description in deep and narrow welds such as the ones produced by means of electron beam or laser beam, a conical heat source model seems to be more suitable. The MHS parameters were already established by the company and are presented in Table 6.4.

<b>Accelerating Voltage</b>	120 kV
<b>Beam Current</b>	12.5 mA
<b>Welding Velocity</b>	20 mm/sec

Table 6.4: MHS parameters.

The experimental weld dimensions represented in Figure 6.10 were also provided by the company. The heat source model parameters that are explained in Section 3.6, Equation 3.8 and Equation 3.9 - namely the conical upper radius, conical lower radius, conical depth and the gaussian parameter were calibrated through sensitivity analysis and are presented in Table 7.8.



Figure 6.10: Experimental weld dimensions.

Main Heat Source	
Conical Upper Radius ( $r_u$ )	0.075 mm
Conical Lower Radius ( $r_l$ )	0.050 mm
Conical Depth ( $d_c$ )	1.565 mm
Gaussian Parameter (M)	3

Table 6.5: MHS Simufact parameters.

**Thermal simulations** were conducted to replicate the experimental fusion zone in Figure 6.10 after calibrating the heat source model parameters. To do this: a short trajectory was chosen and the geometry used for the experiment was a flat plate with 15mm of thickness, 400mm length and 150mm width. The process efficiency values corresponding to different weld dimensions are presented in Table 6.6.

Efficiency [%]	Weld Width [mm]	Weld Depth [mm]
100	0,981	1,494
95	0,933	1,467
90	0,868	1,401
85	0,809	1,363
80	0,734	1,322
75	0,682	1,241
70	0,621	1,165
65	0,558	0,935
60	0,506	0,781
55	0,419	0,513
50	0,390	0,437

Table 6.6: Numerical calibration of process efficiency.

The desired dimensions for the weld were 0,90mm weld width and 1,44mm weld depth. From the previous table, it could be concluded that increasing the efficiency would cause more heat to go towards the fusion zone (as there were less heat dissipation losses), increasing the weld dimensions. A linear interpolation between the values corresponding to an efficiency of 90% and 95% was performed and gave an efficiency of 93.5%. The fusion zone in Figure 6.11 corresponds to a conducted **thermal simulation** for this efficiency value.

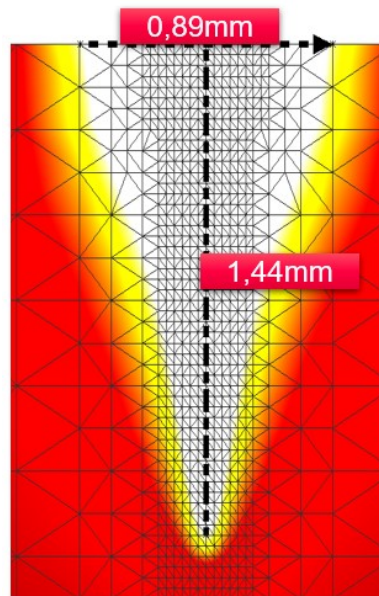


Figure 6.11: Numerical weld dimensions.

In this case, numerically it was possible to successfully replicate the thermal distribution during welding of CuCr1Zr that was provided by the company. The weld had 0.89mm width and 1.44mm depth.

The minor difference in the fusion zone between Figure 6.10 and Figure 6.11, obtained experimentally and numerically, respectively, could be addressed due to slight approximations that were considered when performing sensitivity analysis for the heat source model. Furthermore, the efficiency calibration was fully dependent on the aforementioned analysis.

- **Brief summary**

As a summary of this chapter, a solution for minimizing hot cracking was proposed as the **thermally induced reduction of the load**. Before following the methodology suggested and introducing a SHS, an assessment on the MHS had to be done such that all influential heat source model parameters were known. This was completed using **only thermal simulations** as they greatly reduced simulation time. The numerical implementation of these models was considered reasonably good so, for future reference, they were kept untouched. On the next chapter, **thermomechanical simulations** were directed to evaluate both the temperature distribution and the stresses.

## Chapter 7

# Results and Discussion

Having successfully performed an assessment on the MHS such that all influential heat source model parameters were known, it was possible to evaluate the stress distribution conducting thermomechanical simulations. These simulations allow extraction of the thermal distribution around the fusion zone as well as the magnitude of the stresses. All the results were exported to an Excel file and compared to the temperature dependent proof stress of the material. The criteria proposed in Section 6.3, Equation 6.1 was used to verify if it was possible to avoid hot cracking. The statistical software Minitab 19 [41] was used to obtain an optimal solution for the SHS parameter configuration minimizing the stress to proof stress ratio.

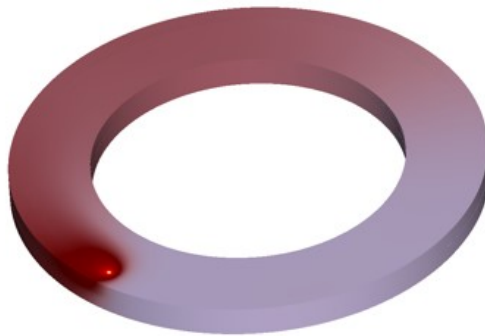


Figure 7.1: Thermomechanical simulation in Simufact Welding.

## 7.1 No Secondary Heat Source

### 7.1.1 Numerical

A thermomechanical simulation without the use of a secondary beam was employed and provided an overview on the residual stresses. This evaluation was performed on points selected aligned with the X-axis and Y-axis (as is shown in Figure 7.2) given that the X-stress and Y-stresses at these points, respectively, are entirely equal to the radial stresses (that cause hot cracking). Moreover, multiple points equally spaced in depth were considered to verify if cracking would, in fact, firstly emerge on the surface of the material.

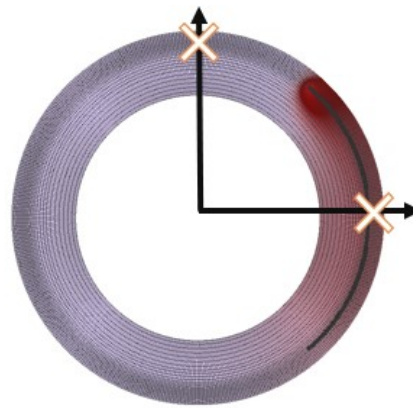


Figure 7.2: Top view on point selection.

Initially it was verified that hot cracking occurred given that the stress applied on the selected points overcame the proof stress at the given temperature for many conducted trials performed in this framework. Since the cracking was occurring first on the surface of the material, it was not necessary to check the stress values for the other points below the surface. The first step for data analysis was to check the temperature distribution in Figure 7.3 on the surface point.

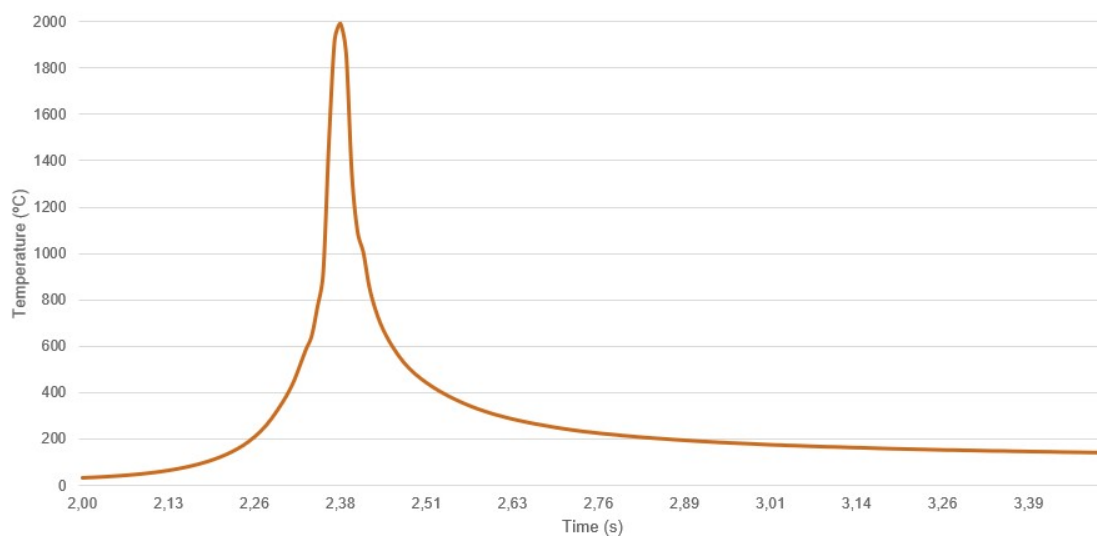


Figure 7.3: Temperature over time on the surface of a pre-select point in the weld line.

### 7.1.2 Experimental

An experimental verification on the rapid solidification ( $1800^{\circ}\text{C}/\text{sec}$ ) was executed using the electron beam machine at TU Graz. Relevant machine benchmarks are presented in the appendix A.1. The results were compared to numerical values obtained from the software. It was important that the thermo-mechanical model built in Simufact did not have much of a difference compared to the real experiment as this would proven vital for the final validation. An experimental simulation was conducted on a copper plate of 20mm thickness to evaluate the high cooling rates. Comparing to the weld dimensions obtained in the simulation; the one attained experimentally yielded a weld width of about 1.05mm (14% relative error). Two different thermoelements T1 and T2 were placed 2mm and 1mm, respectively, away from the center of the weld line. The setup can be seen in Figure 7.4.

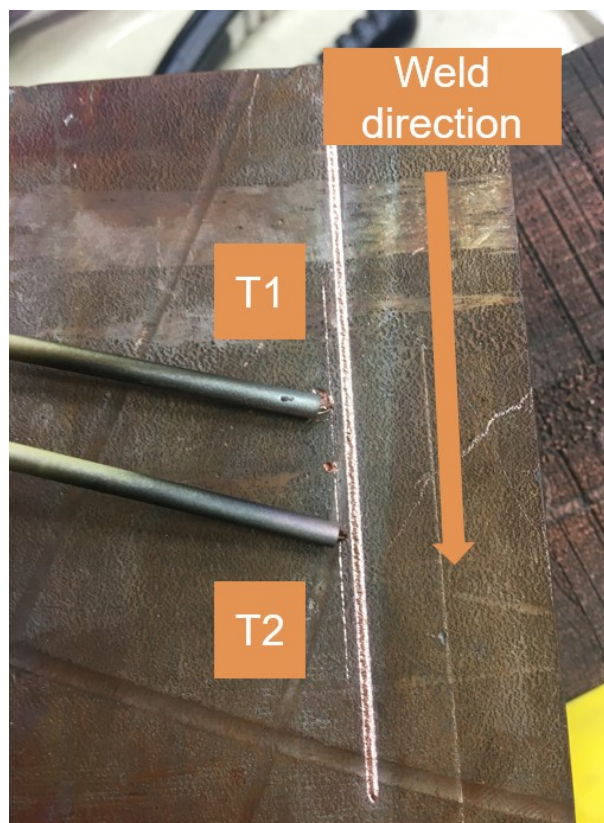


Figure 7.4: Experimental setup.

The max temperatures displayed in Figure 7.5 in the case of T1 and T2 were of about 150°C and 405°C, respectively, **and the key result being that both cooled down to ambient temperature in less than a second.**

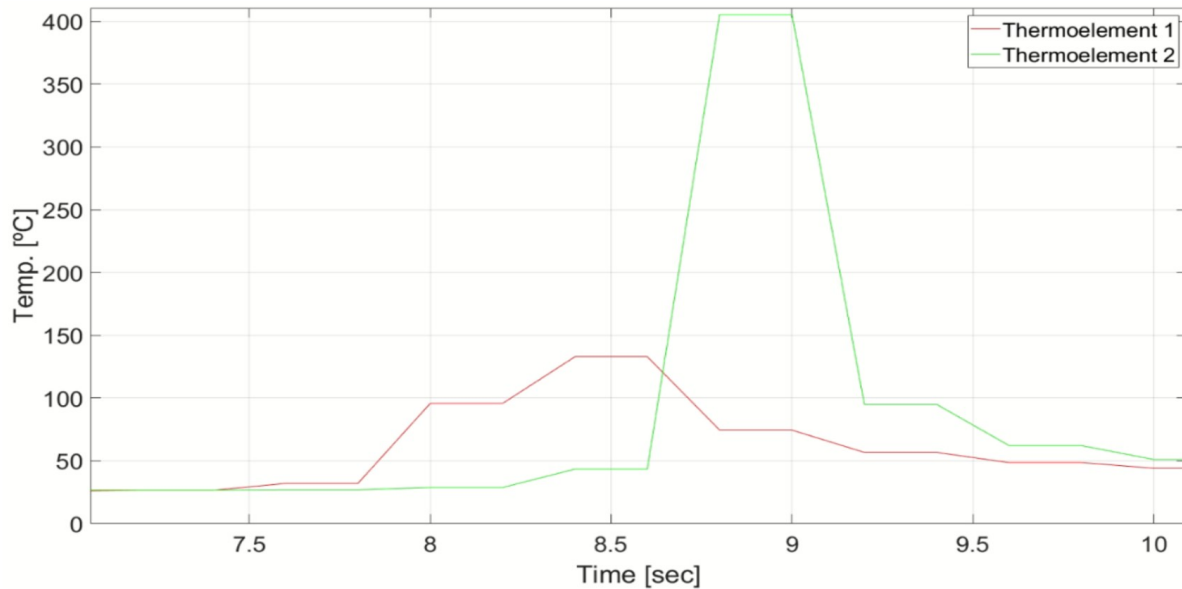


Figure 7.5: Experimental thermal distribution.

The temperature at these points was also verified in the numerical software and the error was about 10%. This difference can be explained mainly due to two specific reasons:

1. **Poor acquisition data** - the thermoelements had a very high discrete sample time so it did not register the heating and cooling rates as accurately as intended.
2. **Material** - the material used was copper and its conditions for the experiment in the laboratory were not exactly the same as the ones considered for the simulation.



The performed thermomechanical simulation provided the results for the stress values over time on the previously defined surface point as shown in Figure 7.6. Moreover, the risk for hot cracking occurred during solidification, so the time window was designated accordingly.

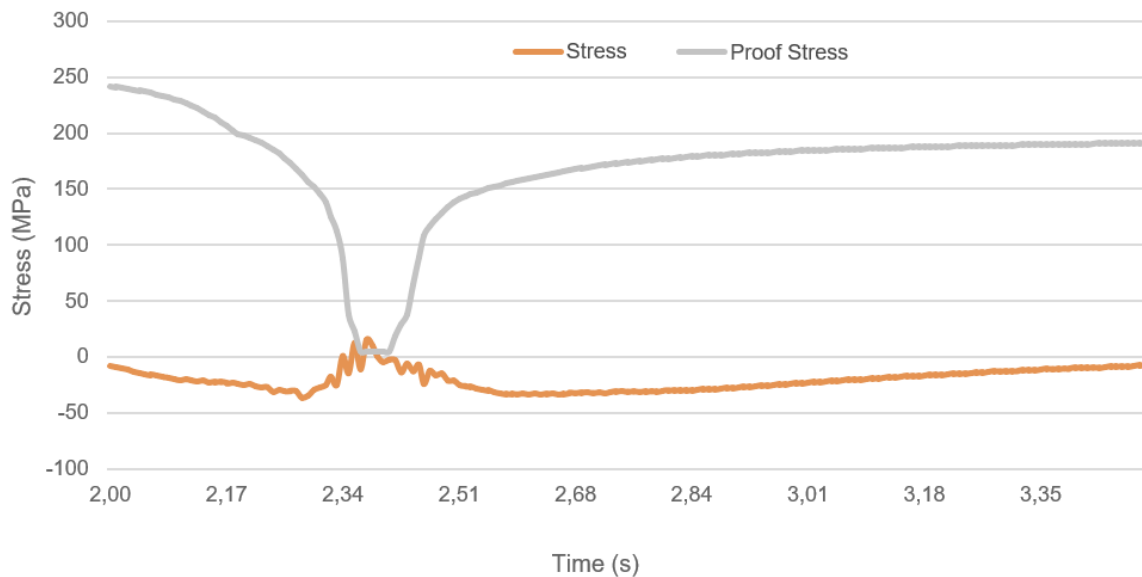


Figure 7.6: Stress evaluation over time on the surface of a pre-selected point in the weld line.

To further understand the ratio between the residual stresses and the proof stress and to ease the evaluation on occurrence of hot cracking, the ratio was also plotted over time as can be seen in Figure 7.7. Hence, it can be acknowledged that cracking occurred since the relation yielded a value greater than 1.

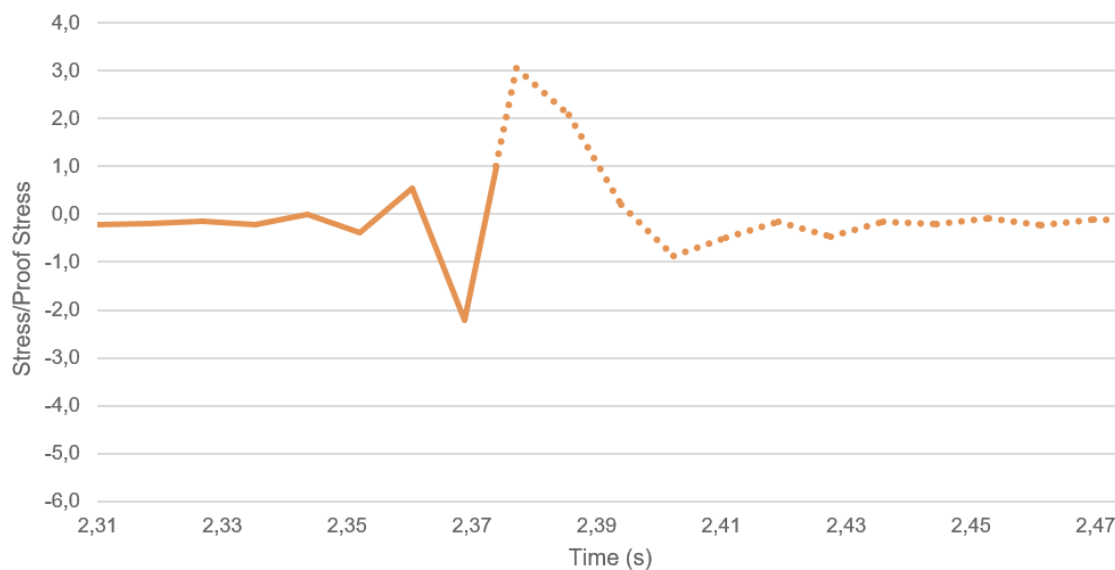


Figure 7.7: Ratio between stress and proof stress over time on the surface of a pre-selected point in the weld line. Dashed line represents case of hot cracking.

## 7.2 One Factor at a Time (OFAT)

A set of arbitrated starting-point values belonging to or imposed upon the variables defined in Subsection 6.4.1 was defined.

- $P = 50\%$
- $d = 1\text{mm}$
- $\alpha = 0^\circ$

It was concluded in Figure 7.8 that utilizing a SHS with those characteristics too close to the MHS would produce a merge in the fusion zone, melting even more material than intended.

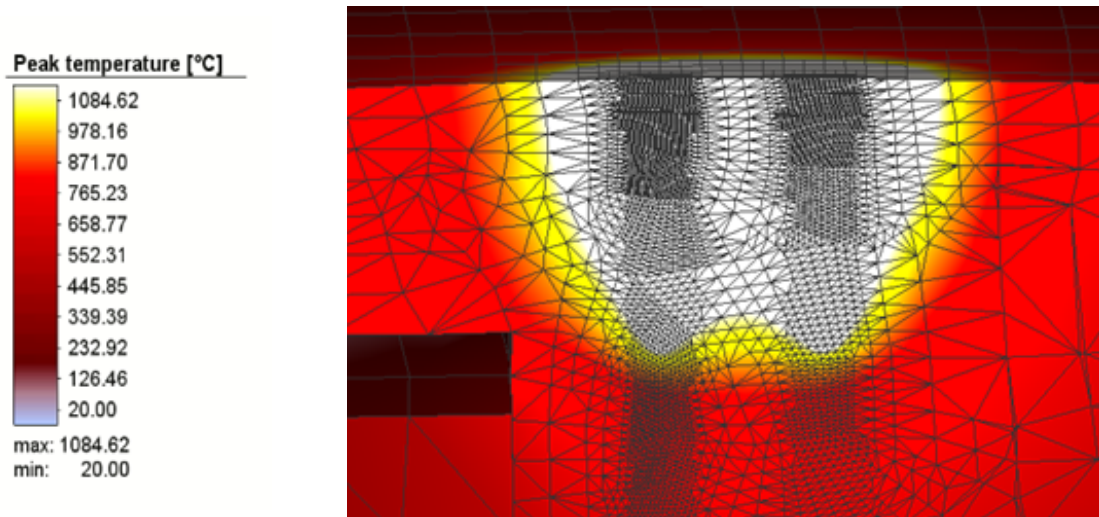


Figure 7.8: Numerical fusion zone for the starting condition.

To avoid melting by the SHS a sensitivity analysis using OFAT, explained in Subsection 6.3, was selected on the Power, keeping all other variables constant. By iteratively lowering the power, it was seen in Figure 7.9 that for this angle and radial distance ( $\alpha = 0^\circ$  and  $d = 1\text{mm}$ ), 2.5% was the maximum power that could be employed without secondary melting.

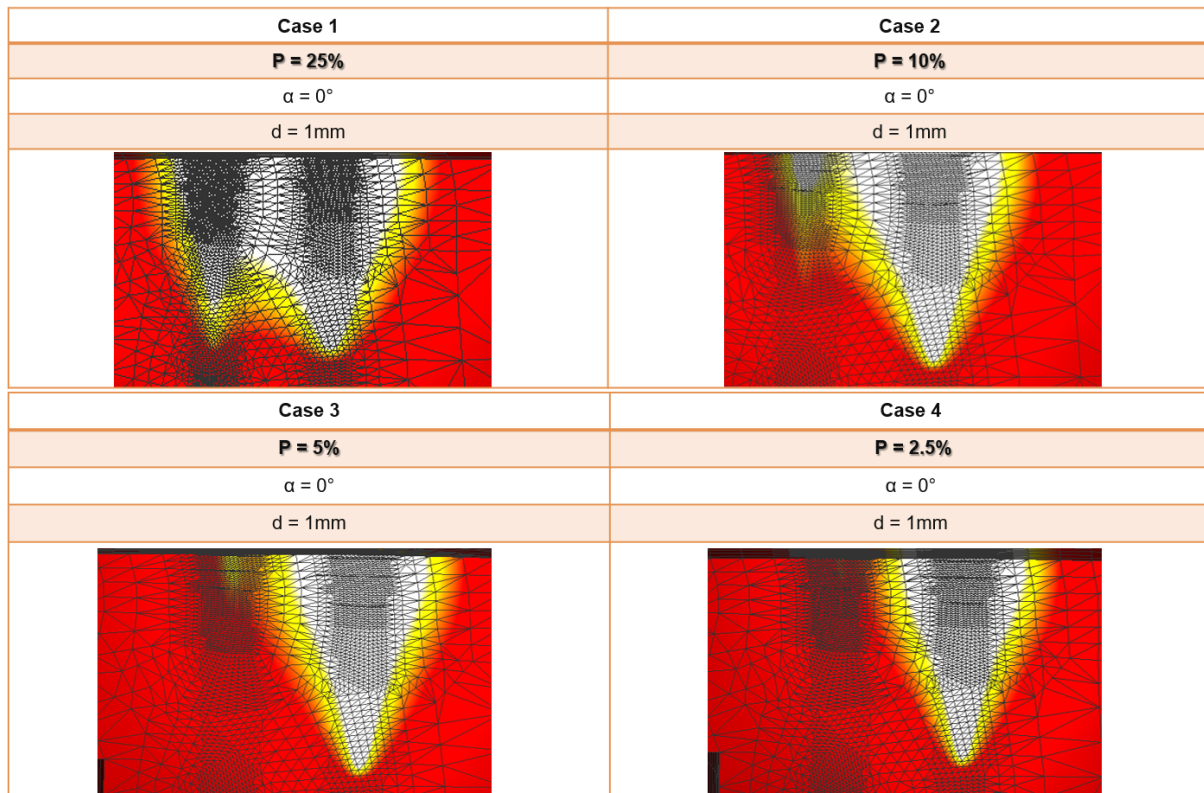


Figure 7.9: Numerical fusion zones for different power values using OFAT approach.

Subsequently, an assessment on the radial distance whilst maintaining other variables constant was performed. The results for the study using OFAT method for the radial distance are presented in Figure 7.10.

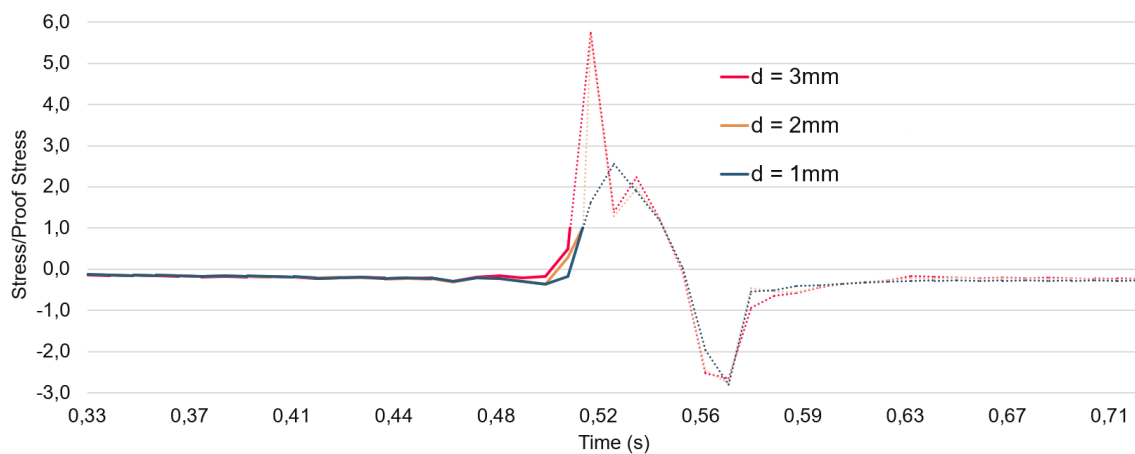


Figure 7.10: Ratio between stress and proof stress over time for different radial distances using OFAT method. Dashed line displays case of hot cracking.

It could be seen that increasing the radial distance would stop changing the outcome of the results, since case of hot cracking was shown for every trial performed. After having performed the OFAT method to the power applied and the radial distance between heat sources, a study on the angle was accomplished. However, since the variation of the angles was very small ( $\sim 0^\circ$ ), for notation simplification purposes, this variable was hereafter described as the tangential distance (dt) allowing for easier understanding. The results are shown in Figure 7.11.

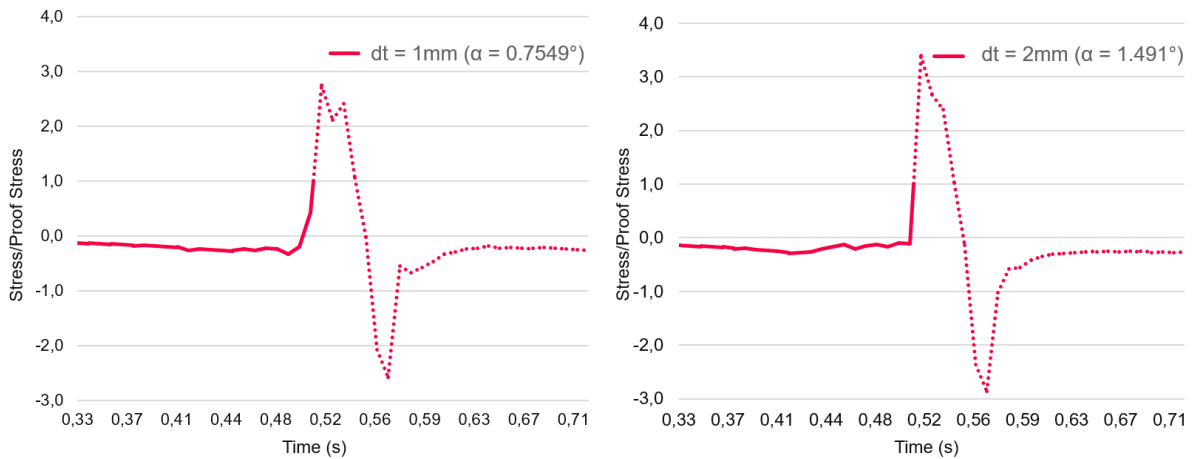


Figure 7.11: Ratio between stress and proof stress over time for two tangential distances using OFAT method. Dashed line represents case of hot cracking.

The tangential distance had a clear impact on the results, the closer the heating sources were, the better the results. This made sense since in this case the cooling rate was very high so there was a need to rapidly introduce compressive stresses. Multiple tests were conducted for surface diameter of the SHS, ranging from as low as  $D = 0.075\text{mm}$  up to as high as  $D = 5\text{mm}$ , but the results did not vary that much. In some experiments (mainly with higher  $D$ ), the computation required was high enough that Simufact had trouble converging to a solution, due to the merging of both heat sources. The power was always adjusted accordingly.

### 7.3 Design of Experiments (DoE)

Having gathered understanding of the impact of each variable on the outcome of the simulations, the next step would be to build a parameter window for the factor levels in DoE. It is an attractive tool to investigate the case of hot cracking under a combination of parameters and different scenarios. Furthermore, it aims to guide to the selection of the proper combination of process parameters at specified levels. Combining FEM and DoE is a modernized way of reducing computational effort. In this thesis, the classical design FFD was selected due to the provided reliability and capacity of giving information on how each factor was correlated with each other.

A 3-level full factorial DoE with 4 factors was initially chosen, Table 7.1. Thus, a total number of 81 simulations were conducted to perform the statistical analysis.

Factor	Levels	Level 1	Level 2	Level 3
d [mm]	3	2	3	4
P [%]	3	35	40	45
dt [mm]	3	-3	-1	1
D [mm]	3	2	3	4

Table 7.1: 3-level full factorial DoE with 4 factors.

Visual analysis tool Pareto charts were used to gauge statistical importance of each interaction to the response. In this way the chart visually depicts which situations are more significant by their length (bigger the better). Thus, it was verified that the tangential distance had a meaningful impact on the outcome. In this case, the standard error of regression and the  $R^2$  values were also taken into account for model evaluation. Removing irrelevant interactions, below a 5% level of significance, led to results presented in Figure 7.12.

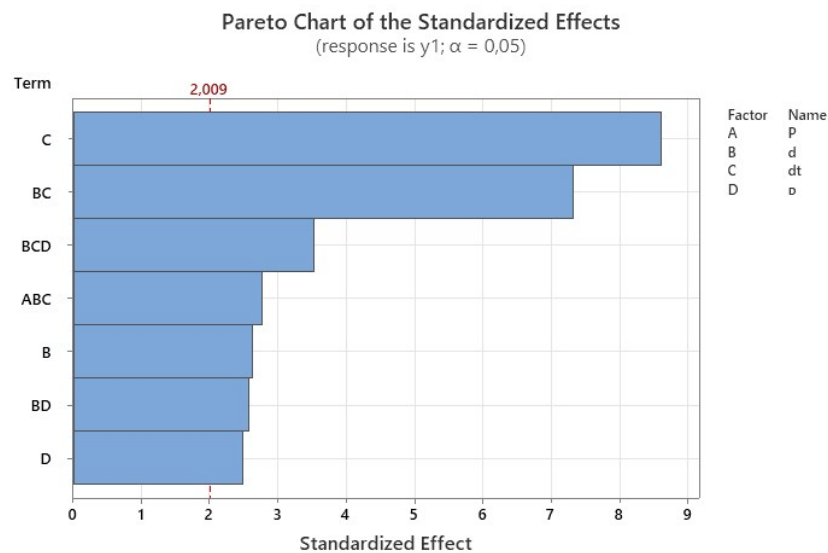


Figure 7.12: Pareto chart for the standardized response of the initial DoE for  $\alpha = 5\%$ .

The influence of each individual factor on the ratio between stress and proof stress is indicated in Figure 7.13. It could also be seen that most factors kept the ratio constant (with slight deviations) aside from the tangential distance. This concluded that the tangential distance had a clearer impact on the outcome and readjusting the levels of other factors would probably help achieving better results. In a similar fashion, it could also be expressed in Figure 7.14 that there was not an optimal factor configuration that numerically solved the problem (stress/proof stress  $< 1$ ) for the initially chosen DoE.

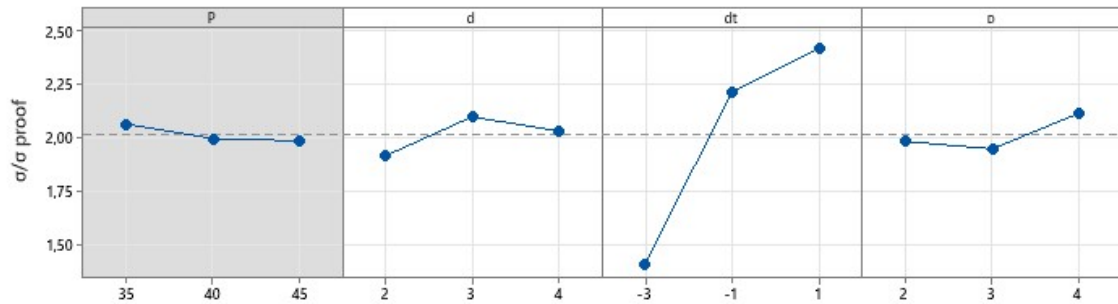


Figure 7.13: Fitted means for each factor for the initial DoE.

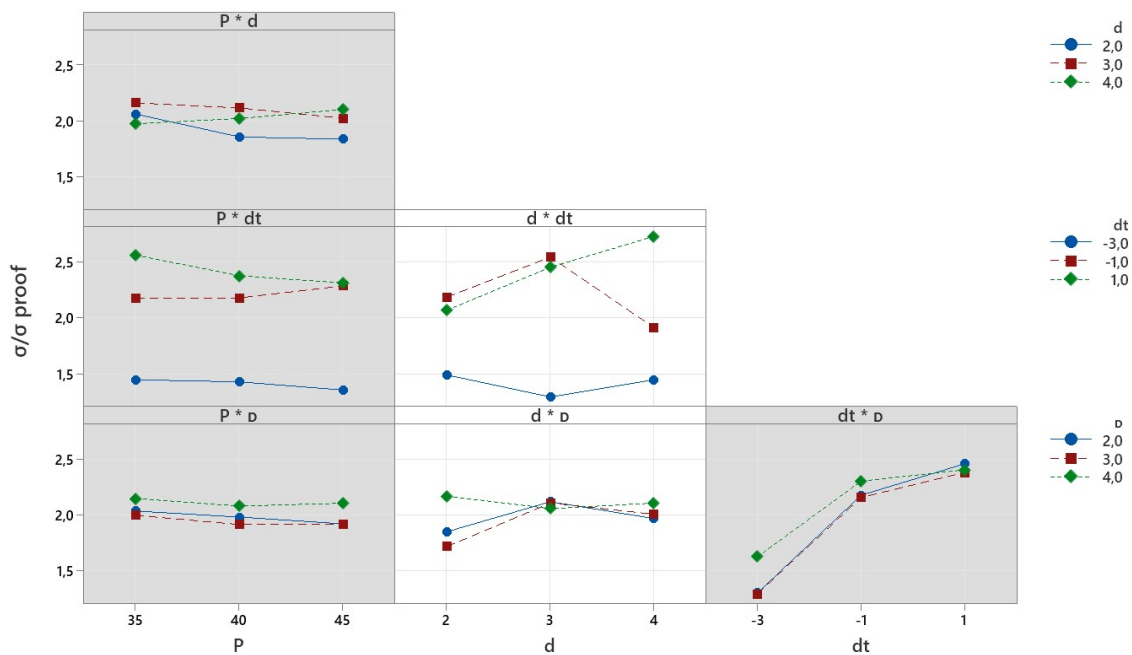


Figure 7.14: Influence on the response based on the interactions between factors for the initial DoE.

ANOVA results are presented in Table 7.2. Within this verification, the F-value was used for comparing the factors of the total deviation and the p-value was accounted for the contribution of each parameter in this process. 5% was considered to be the level of significance.

Source	Degrees of Freedom	Adj SS	Adj MS	F-Value	p-Value
Model	30	23,032	0,768	16,31	0,000
d	2	0,458	0,229	4,87	0,012
dt	2	15,337	7,669	162,94	0,000
D	2	0,418	0,209	4,44	0,017
d. dt	4	3,512	0,878	18,65	0,000
d. D	4	0,0662	0,165	3,52	0,013
P. d. dt	8	1,129	0,141	3,00	0,008
d. dt. D	8	1,516	0,189	4,03	0,001
Error	50	2,353	0,047		
Total	80	25,385			

Table 7.2: ANOVA for the initial DoE.

To improve the first attempt, ANOVA also resulted on the identification and elimination of irrelevant factors and levels. Hence, the surface diameter of the SHS was dropped and a modified 2-level DoE with 3 factors, displayed in Table 7.3, was carried out. The tangential distance levels were considered at levels  $dt = 3.5$  mm and  $dt = 3$  mm and the radial distance levels were  $d = 2$  mm and  $d = 2.5$  mm since these yielded the best results. The power levels were increased to 45% and 50% because increasing the power seemed to reproduce better results. However, increasing it even more would lead to melting by the SHS, so these values were adjusted to match both distances appropriately.

Factor	Levels	Level 1	Level 2
d [mm]	2	2,0	2,5
P [%]	2	45	50
dt [mm]	2	-3,5	-3,0

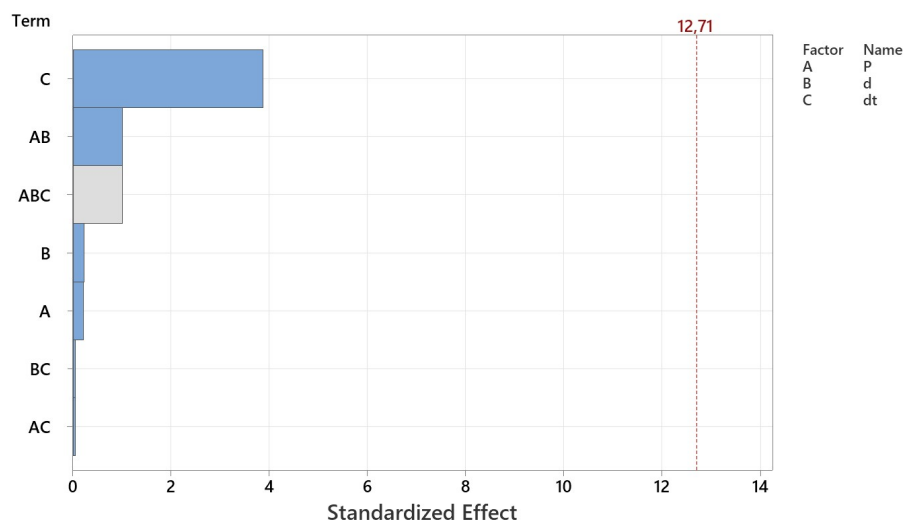
Table 7.3: 2-level full factorial DoE with 3 factors.

The statistical results are presented in Table 7.4. Despite fitting well to the provided data (reasonable  $R^2$ ), the model had a poor predicted  $R^2$ .

S	$R^2$	$R^2$ (adjusted)	$R^2$ (predicted)
0,2378	94,14%	58,95%	0,00%

Table 7.4: Tweaked DoE statistical results.

Again, Pareto chart shown in Figure 7.16 was used to provide a visual overview on the significance of the interactions to the response for a specified threshold.

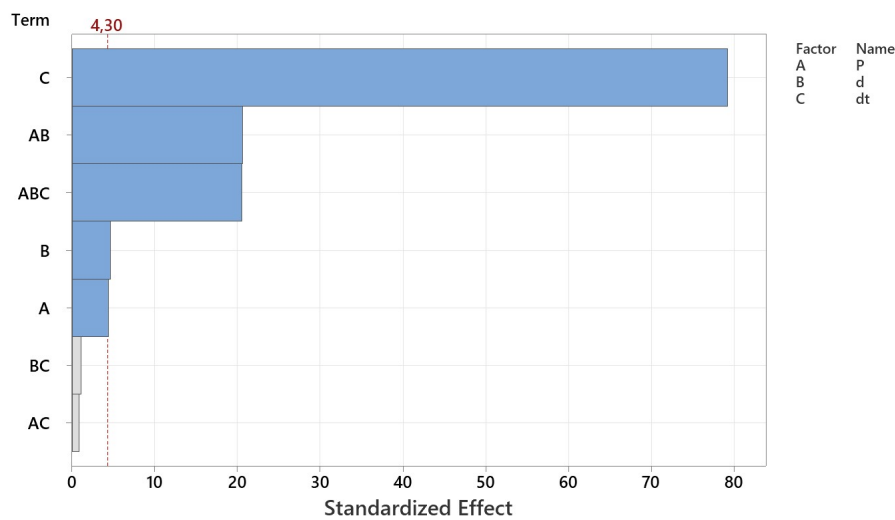
Figure 7.15: Pareto chart for the standardized response of the tweaked DoE for  $\alpha = 5\%$ .

The modified DoE was further improved from the analysis of the previous Pareto chart of standardized effects for a significance level of 5% presented in Figure 7.16 and the ANOVA displayed in Table 7.5. Therefore, all the unnecessary factors and interactions were also removed (for instance, interaction between tangential distance and both radial distance and power – AC and BC).

Source	Degrees of Freedom	Adj SS	Adj MS	F-Value	p-Value
Model	5	0,964	0,193	1429,65	0,001
P	1	0,003	0,003	19,38	0,048
d	1	0,003	0,003	21,59	0,043
dt	1	0,845	0,845	6263,56	0,000
P. d	1	0,057	0,057	424,36	0,002
P. d. dt	1	0,057	0,057	419,36	0,002
Error	2	2,353	0,047		
Total	7	25,385			

Table 7.5: ANOVA for the modified DoE.

The Pareto chart corresponding to the modified DoE model is expressed in Figure 7.16. It can be seen that all interactions of interest were above a certain threshold.

Figure 7.16: Pareto chart for the standardized response of the modified DoE for  $\alpha = 5\%$ .

The statistical results for model evaluation are presented in Table 7.6. The model obtained had an excellent  $R^2$ ,  $R^2$  adjusted and predicted  $R^2$  values.

S	$R^2$	$R^2$ (adjusted)	$R^2$ (predicted)
0,01	99,97%	99,90%	99,55%

Table 7.6: Modified DoE statistical results.

The impact of each variable individually could be analysed through the main effects plot for the response as seen in Figure 7.17. In comparison to the first DoE model, it was also possible to conclude that the tangential distance had a bigger influence on the outcome compared to the other variables.



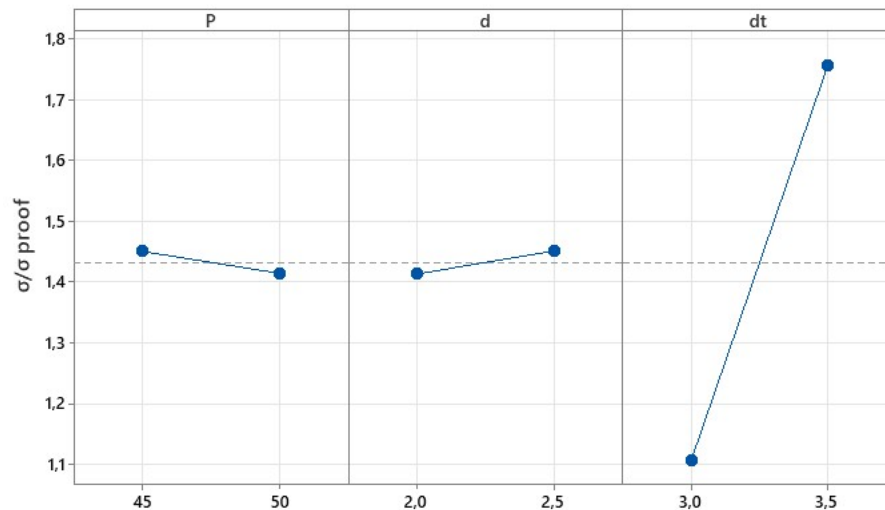
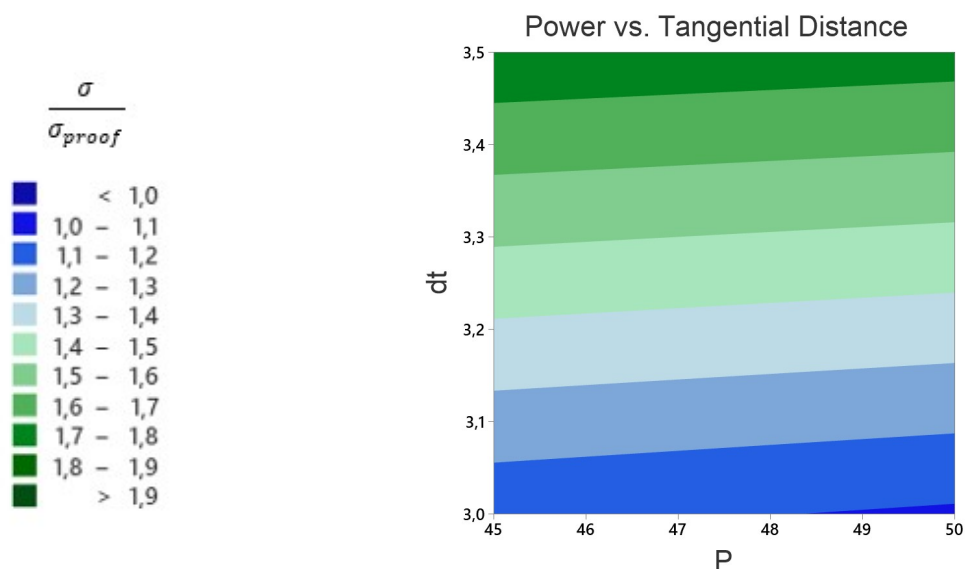
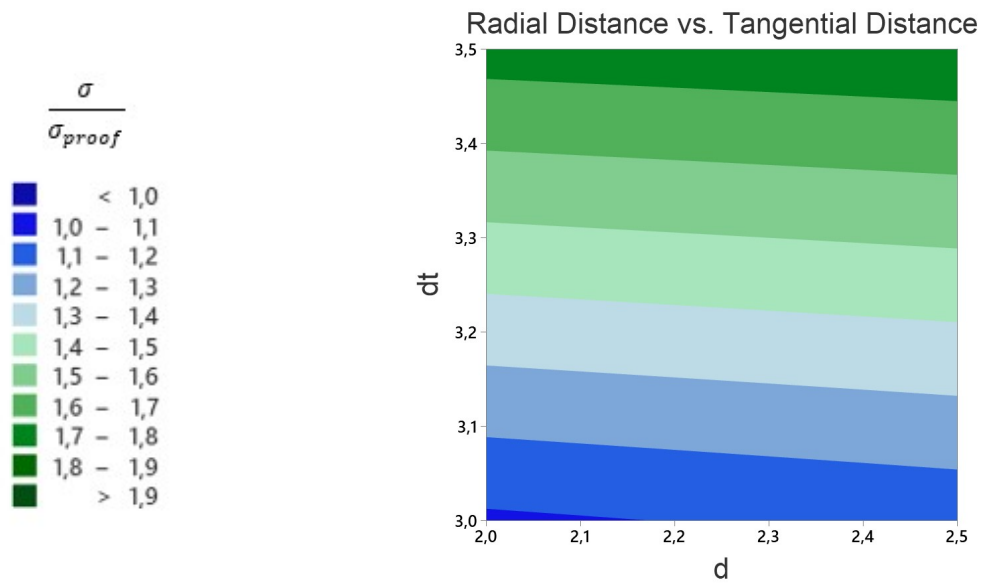


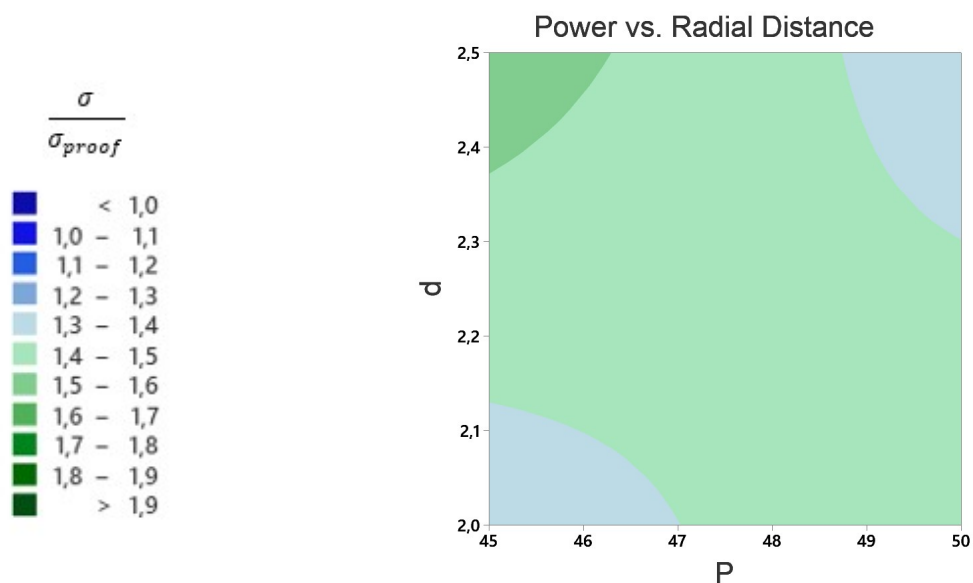
Figure 7.17: Fitted means for each factor for the modified DoE.

The interactions between factors were extracted and evaluated through contour plots and are descriptively presented. Since they were 2-variable plots for a 3-factor DoE, one of the factors was held at constant value so that it would be possible to analyze the plots separately. In this case, the held value was picked as the average value between levels available. Figures 7.18 and 7.19 show that the response ratio (to be minimized) was not changing on the X-axis (P and d) meaning that this variable compared to Y-axis variable (dt) was inconsequential.

Figure 7.18: Response vs. P. dt — **Held value** d = 2,25 mm.

Figure 7.19: Response vs. d. dt — **Held value** P = 47,5%.

In spite of improvements to the model, it was also revealed by Figure 7.20 that there was still not an optimal region for the hot cracking problem.

Figure 7.20: Response vs. P. d — **Held value** dt = 3,25 mm.

The held values being the average between levels were not a good fit. Subsequently, experiments accounting for different held values were conducted and the corresponding contour plots can be seen in Figure 7.21, Figure 7.22 and Figure 7.23.

The relationship amongst the tangential distance between both heat sources and the Power, while holding the radial distance at a specified value of 2 mm (chosen from the DoE) is characterized in Figure 7.21. Conducting experiments with a combination of smaller tangential distances and power applied proven to be beneficial. Similarly to previous Figure 7.18 that also related the response with respect to the power and tangential distance, it could be concluded that the power was proven inconsequential for higher values of  $dt$  given that the response maintained a certain value. **However**, the power displayed greater impact for smaller values of  $dt$ .

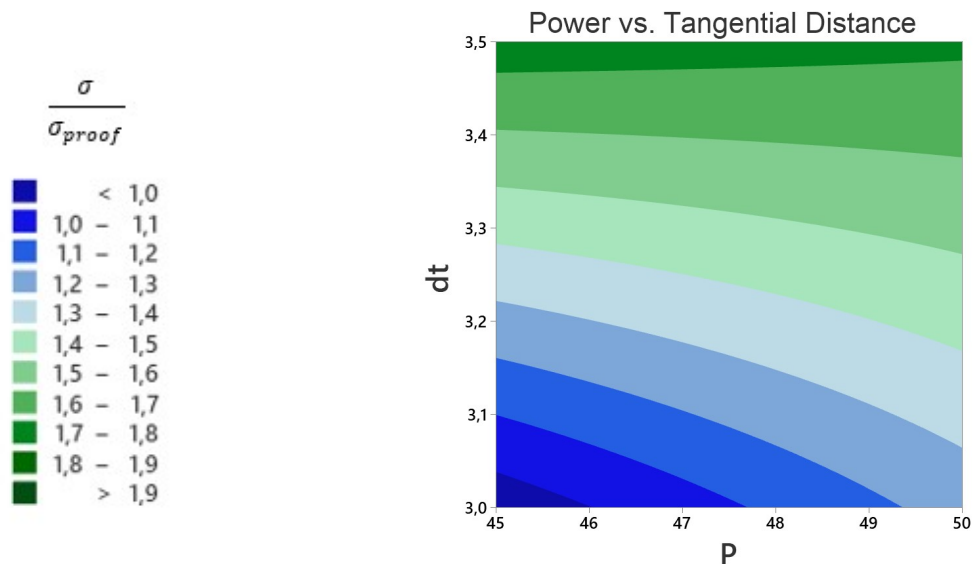


Figure 7.21: Response vs. P. dt — **Held value**  $d = 2$  mm.

The effect on the response considering the distance of both heat sources while keeping the power at a constant value of 50% (chosen from the DoE) is presented in Figure 7.22. Conclusively, the radial distance displayed greater impact for lower values of the  $dt$  while being irrelevant for higher values of  $dt$ .

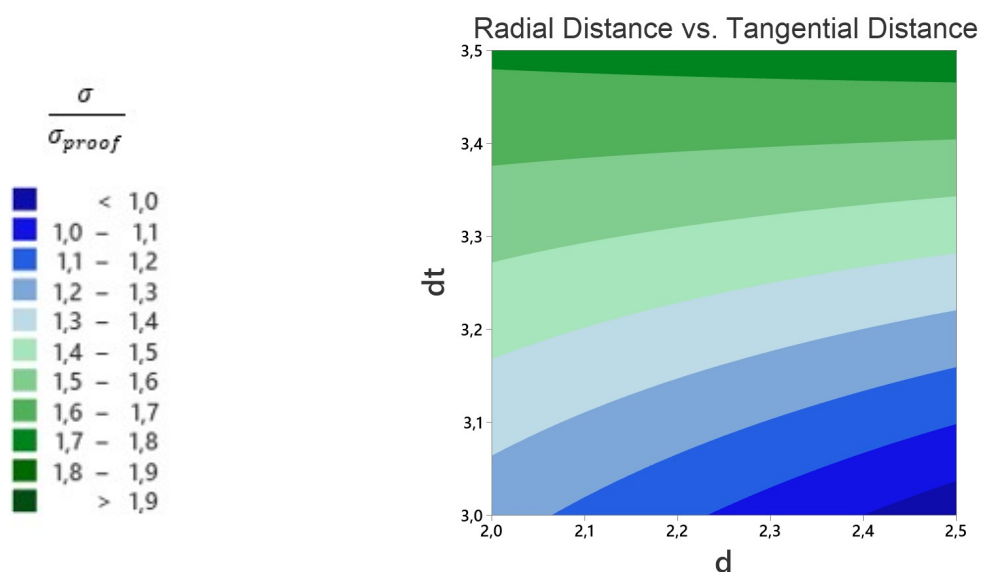


Figure 7.22: Response vs. d. dt — **Held value**  $P = 50\%$ .

An interesting result could be extracted from the contour plot on Figure 7.23 which relates the radial distance between heat sources and the power applied while maintaining the tangential distance constant at 3mm. The results improved with a relative increase in power and radial distance – increasing power required a higher distance between both heat sources; whereas a lower power would allow a smaller distance between both heat sources to reproduce similar satisfactory results. This made sense given that when the temperature is near the melting temperature, the results worsened.

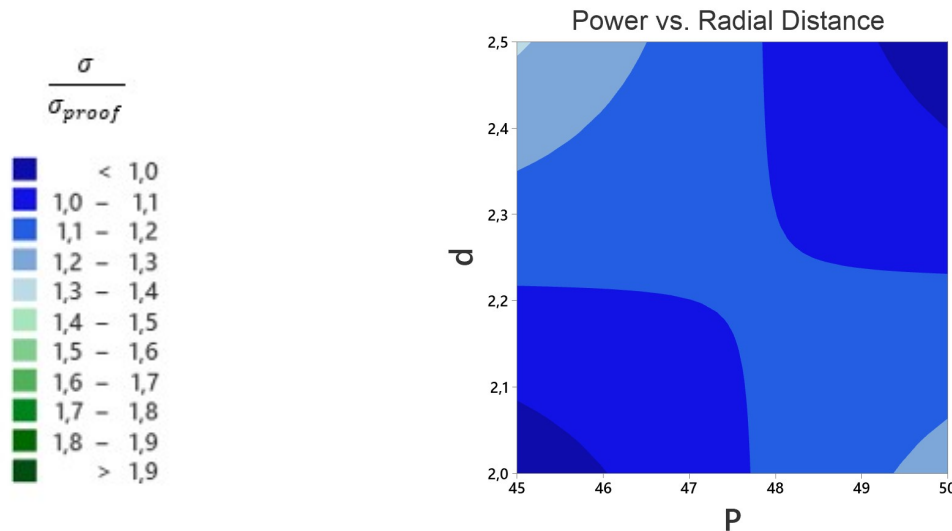


Figure 7.23: Response vs. P. d — **Held value** dt = 3 mm.

## 7.4 Verification and Validation

It was necessary to determine whether the DoE model implementation and its associated data accurately represent the conceptual methodology and specifications. The model response is given by the following LR Equation 7.1.

$$Y(P,d,dt) = 1,43158 - 0,01807P + 0,01907d + 0,32493dt - 0,08458 P \cdot d + 0,08407 P \cdot d \cdot dt \quad (7.1)$$

The response optimizer in Minitab allows to identify the combination of input variables that optimize a single response based on their weighted importance [57–59]. In this case Equation 7.1 was to be minimized. The results showed significant improvement when compared to the first trials, there were multiple feasible solutions from which hot cracking could be mitigated as seen in Table 7.7. Promising parameter combinations were from 1 to 5.

Solution	P [%]	d [mm]	dt [mm]	$\frac{\sigma}{\sigma_{proof}}$
1	45,00	2,00	-3,00	0,9370
2	50,00	2,50	-3,00	0,9390
3	49,99	2,49	-3,00	0,9415
4	45,21	2,00	-3,01	0,9522
5	50,00	2,47	-3,00	0,9529
6	45,98	2,40	-3,00	1,1907
7	45,07	2,49	-3,00	1,3012
8	50,00	2,00	-3,50	1,7199

Table 7.7: Solutions for the minimization of the ratio between stress and proof stress.

Numerical validation was carried to assess the adequacy of the statistical model, thus condition 1 was selected for a final experiment as can be seen in Figure 7.24. The peak temperature of the SHS at different times throughout the simulation was 1020°C. Weld dimensions were respected.

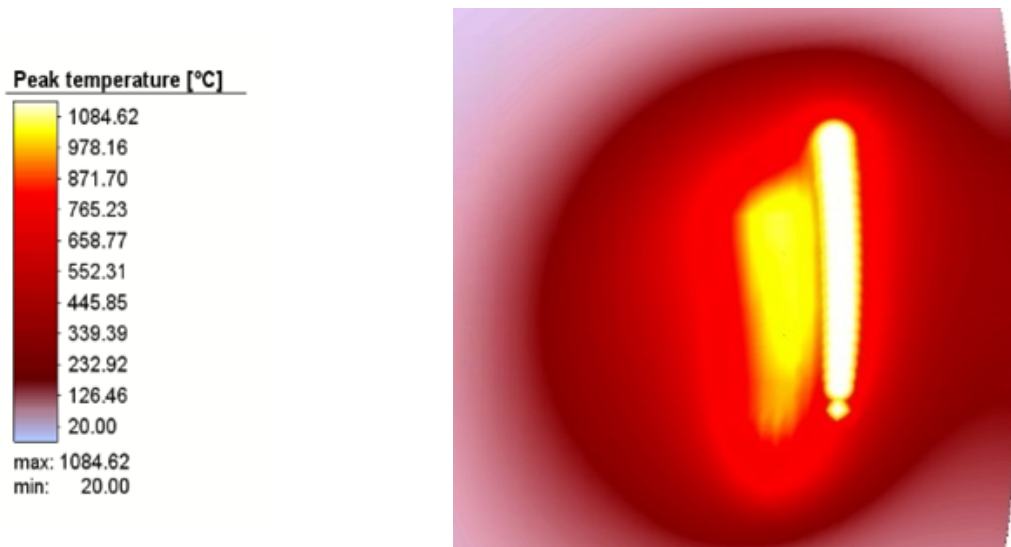


Figure 7.24: Visual representation of the peak temperature at different times.

As it is seen in Figure 7.25, hot cracking did not seem to occur (stress/proof stress <1) under these conditions, so a solution was found and thus, confirming that the TIRL method is suitable to avoid hot cracking in CuCr1Zr.

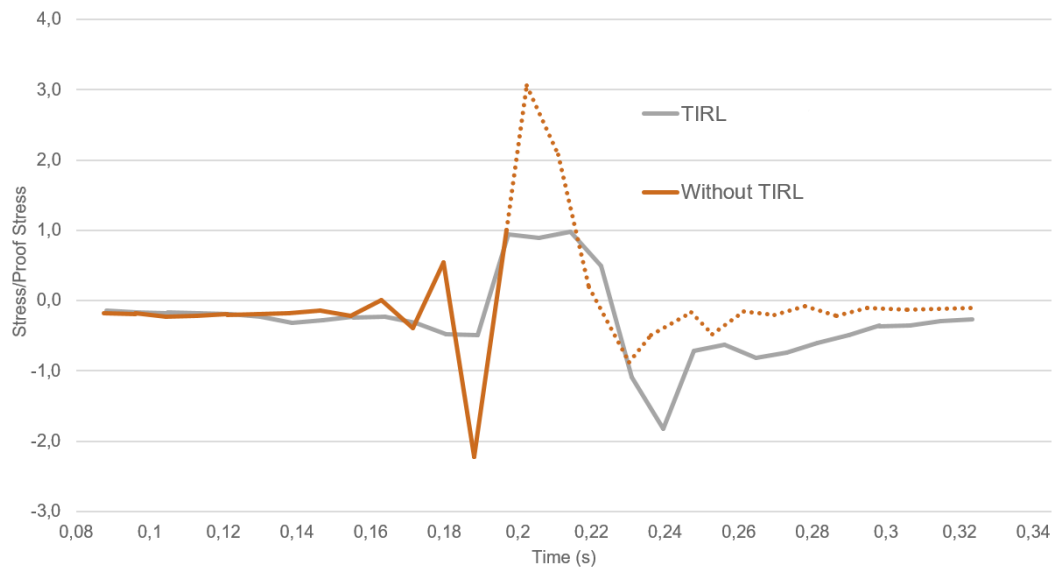


Figure 7.25: Stress evaluation over time on the surface of a pre-selected point with and without TIRL. Dashed line indicates case of hot cracking.

## 7.5 Support Vector Machine (SVM)

A different approach was issued using the SVM algorithm. The following results were extracted using the scikit-learn library in Python (one of the most famous libraries for Machine Learning algorithms and also for pre-processing steps).

All previously conducted simulations were used to build this model. A total of 81 data samples were collected. Initially, 4 variables were considered. However, secondary beam diameter,  $D$ , was considered negligible during previous trials, therefore it was fixed for a set value of  $D = 3\text{mm}$ , restraining the amount of data samples that were available down to 67. In this manner, it was also possible to visually represent the data in a tridimensional plot as can be verified in Figure 7.26.

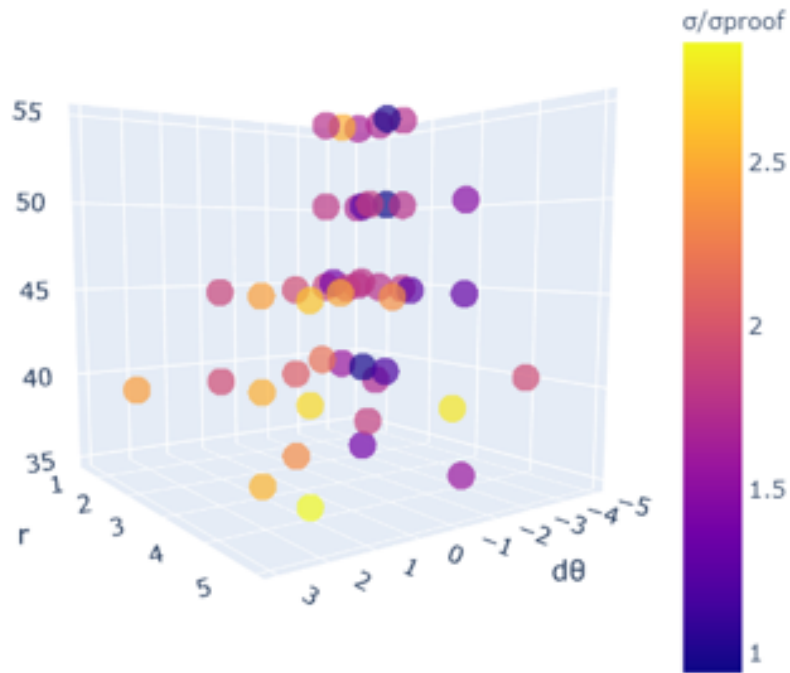


Figure 7.26: Stress/proof stress ratio for all considered data samples.

Subsequently, it was also possible to represent the aforementioned data points (which took the stress/proof stress ratio into account) into a different plot that considered whether cracking occurred or not. In this particular case and as can be seen in Figure 7.27, the classification problem is unbalanced since there are only 4 points of interest (where cracking does not occur).

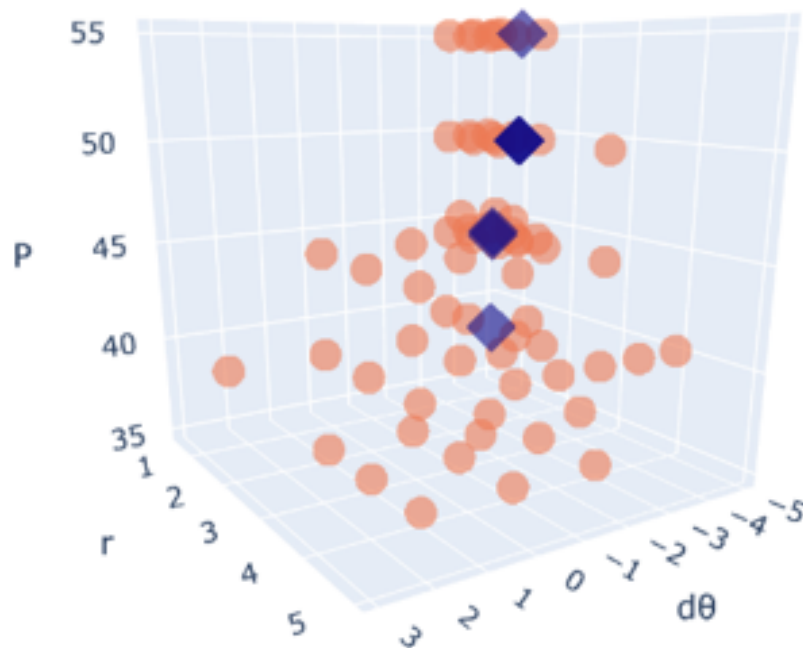


Figure 7.27: Cracking condition for all considered data samples.

Afterwards, a generic SVM model was selected. The regularization parameter  $C$  which is used as the penalty parameter of the error term must not be very high due to overfitting reasons and not too small (due to underfitting). Hence, this parameter needed to be carefully adjusted. The model behaved in a non-linear way, so for proper accuracy of the model, the polynomial kernel was chosen for the boundary condition. Thus, no gamma parameter (defining curvature) was required for the model. The goal was always to find the balance between “not too strict” and “not too loose”.

Later, the data sample was split into training and testing. In this case, 67% of the data was considered for the training the model, whilst the remaining for testing. The confusion matrix obtained is represented in Figure 7.28.

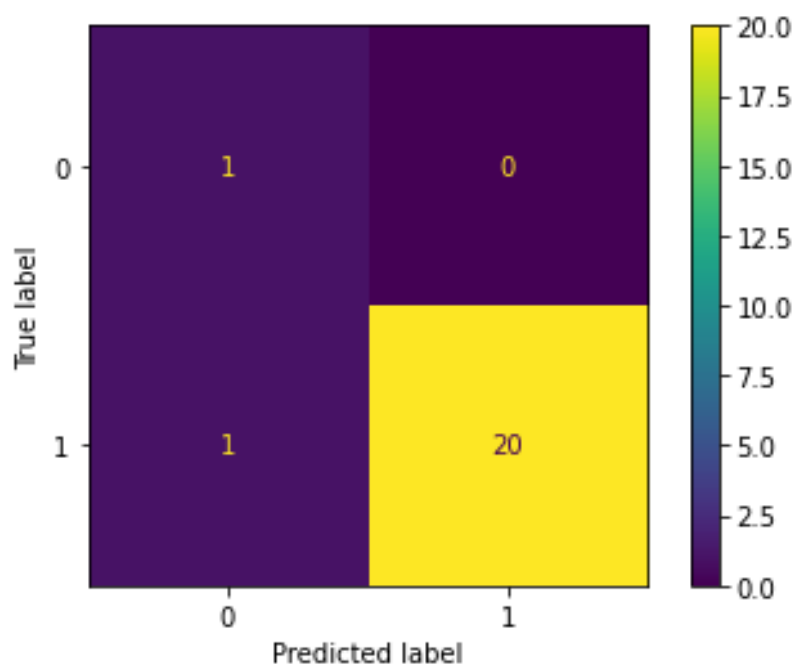


Figure 7.28: Confusion matrix.

In this case, the results were not satisfactory despite the fit being good for the model (accurately predicting the outcome for most testing samples yielding an approx. 95% fit). However, it was seen that in one of the cases, the model predicted that there was no cracking occurring when, in reality, that was not the case. Logically, this would have to be the worst case scenario, so this was not a good model.

Alternatively, a case of undersampling was also tested. The idea was to solve the unbalanced classification problem by selecting the same amount of points with and without cracking. However, this also did not solve the problem.



The unbalanced classification and the limited available data created the need for generalization through cross-validation which is a powerful tool that measures the model's efficiency scores for selecting the best model for a given task. There are a lot of different techniques that may be used to cross-validate a model. Nevertheless, and for this case, the leave-one-out cross-validation was conducted.

The greatest advantage of leave-one-out cross-validation is that it does not waste much data. Only one sample from the whole data set is used as a test set, whereas the rest is the training set as can be seen in Figure 7.29. In this case, a 67-fold cross-validation was considered. While it might be more computationally expensive to perform such tests, this assessment provides an insightful answer to the feasibility of the model.

```

TRAIN: [ 0  1  2  3  4  5  6  7  8  9 10 11 12 13 14 15 16 17 18 19 20 21 22 23
24 25 26 28 29 30 31 32 33 34 35 36 37 38 39 40 41 42 43 44 45 46 47 48
49 50 51 52 53 54 55 56 57 58 59 60 61 62 63 64 65 66] TEST: [26]
Accuracy: 98.48%
MSE: -1.52%
Precision: 92.42%
Recall: 92.42%

TRAIN: [ 0  1  2  3  4  5  6  7  8  9 10 11 12 13 14 15 16 17 18 19 20 21 22 23
24 25 26 28 29 30 31 32 33 34 35 36 37 38 39 40 41 42 43 44 45 46 47 48
49 50 51 52 53 54 55 56 57 58 59 60 61 62 63 64 65 66] TEST: [27]
Accuracy: 100.00%
MSE: 0.00%
Precision: 93.94%
Recall: 93.94%

```

Figure 7.29: Leave-one-out cross-validation.

In the previous figure, and to evaluate the model built, certain cross-validation results such as: accuracy, precision and recall were extracted from each conducted experiment. A single measure to compare between models was taken from the average scoring across all experiments.

Leave-one-out cross-validation scoring	
Accuracy	98.48%
MSE	1.52%
Precision	92.42%
Recall	92.42%

Table 7.8: Leave-one-out cross-validation scoring results.

Across all experiments, the precision or positive predictive value which displays the the ratio of correct positive predictions over the total predicted positives was, on average, equal (92.42%) to the recall or true positive rate which considers the ratio of correct positive predictions over the total positive examples.

The key point with SVM models is that they do not rely on a larger training data sample as the DoE meaning that they could reproduce similar satisfactory results with much less data available, improving time efficiency. Moreover and also unlike DoE, SVM models are much less prone to overfitting (in the case of DoE, the model was heavily tuned to provide the best results) as it is also one of its advantages: to "think outside the box" when using relatively small training data samples.

## Chapter 8

# Conclusions

The main conclusions arising from the work done in the framework of this thesis are presented and categorized according to the issues addressed. A thorough numerical study to avert hot cracking utilizing statistical tools such as DoE and SVM yielded a solution, but due to the characteristics of the problem, namely the very rapid cooling rate of this alloy, it is uncertain that this solution is globally optimal.

### 8.1 Achievements

1. The thermomechanical model built managed to numerically replicate the experimental conditions obtained in the laboratory of the company;
2. A methodology and criteria provided with the DoE, SVM and OFAT methods was established;
3. The influence of each parameter individually and amongst each other was assessed based on the stress magnitude alteration. Given the parameters chosen for the SHS, it was seen that the tangential distance (or angle) between both heat sources had the greatest impact on introducing compressive stresses during solidification while the diameter of the SHS had the least impact;
4. Enhancement of the classical DoE models was performed to achieve feasible solutions for minimizing hot cracking;
5. A supervised machine learning algorithm SVM was built to improve time efficiency providing satisfactory results;
6. Smaller distances between heat sources or higher power for the SHS could cause fusion of the material (and possible merge of the fusion zones);
7. Longer distances between heat sources were proven to be meaningless, given that solidification in this specific alloy occurred very fast;
8. The work performed confirms that numerically it is possible to reproduce electron beam welds in CuCr1Zr whilst avoiding the occurrence of hot cracking using TIRL method.
9. A scientific article publication on the International Journal of Advanced Manufacturing Technology

## 8.2 Undergoing and Future Work

Despite the work performed, there is still work that needs to be addressed and alternatives that may enhance the results.

1. Experimental validation of the numerical approach.
2. Further comparison between the DoE and SVM (or other Machine Learning algorithms).

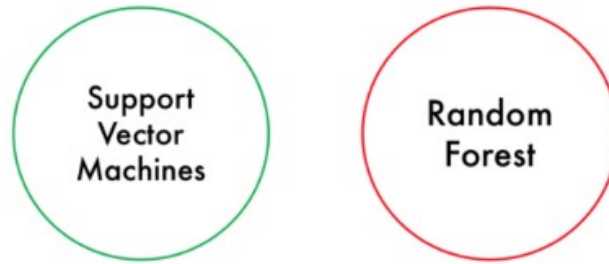


Figure 8.1: Support vector machine vs. Random forest

SVM provided reasonable results, but it would be of interest to evaluate whether it would be practical to use this model instead of the DoE which, despite being more computationally expensive (and requiring more time to gather data for training the model), it still provides the most detailed overview on the outcome of each individual variable and cross-interactions.

3. Conduct more simulations near the interest region in hopes of obtaining more results where cracking does not occur. This, in turn, would improve the SVM model and make it less of a unbalanced classification problem.
4. Use of different types of FEM configuration (types of elements, number of elements, solver..).
5. Implement a different DoE such as the CCD.

# Bibliography

- [1] J. Goldak and M. Akhlaghi. *Computational welding mechanics*. Springer, 2005.
- [2] G. R. Liu and S. S. Quek. *Finite Element Method: A Practical Course*. Elsevier Ltd, may 2003. ISBN 9780080472768. doi: 10.1016/B978-0-7506-5866-9.X5000-2.
- [3] G. Q. Low stress no distortion welding based on thermal tensioning effects. *The Paton Welding Journal*, pages 55–62, 2018.
- [4] I. P. M. M. Wibowo H, Ilman M. Reducing distortion and residual stress using dynamically controlled low stress no distortion and its influence on fatigue crack growth properties of steel welded joints. *Transactions of the Indian Institute of Metals*, 72:143–153, 2019.
- [5] *Electron Beam Welding. Technical Sheets*. EWF, European Welding Federation.
- [6] Principles of electron beam welding. URL <https://www.keyence.com/ss/products/measure/welding/electron-beam/mechanism.jsp>.
- [7] C. Wiednig. Electron beam welding alloy 625. .
- [8] C. Wiednig. Master Thesis Electron Beam Welding Alloy 625 . .
- [9] R. Mitchell. Material properties and microstructures of electron beam welding similar and dissimilar titanium alloys. 144:29–39, 2011.
- [10] S. L. Thomas E. Yost. Effects of select parameters on electron beam welding of al6061-t6 alloy. 2015.
- [11] D. A. L. J. B. J. Saadlaoui Y, Feulvarch É. A new strategy for the numerical modeling of a weld pool. 346, 2018.
- [12] ISO 15609-3(EN). Specification and qualification of welding procedures for metallic materials — welding procedure specification — part 3: Electron beam welding. Standard, International Organization for Standardization, 2004.
- [13] ISO/TR 17671-7(EN). Welding — recommendations for welding of metallic materials — part 7: Electron beam welding. Standard, International Organization for Standardization, 2004.
- [14] Z. L. W. D. J. Weillie Zhou, Robert P. Apkarian. Fundamentals of scanning electron microscopy. pages 1–40, Jan. 2006.

- 
- [15] M.-R. S. Ponce A. and Y. M. Scanning transmission electron microscopy methods for the analysis of nanoparticles. *Methods in Molecular Biology*, 906:453–471, 2012. doi: 10.1007/978-1-61779-953-2\_37.
- [16] H. Schultz. Welding parameters and advice on welding practice. *Electron Beam Welding*, 1993.
- [17] G. Schubert. Electron beam welding process, applications and equipment.
- [18] A. P. S. A. L. G. A. Y. M. V. K. Dragunov, E. V. Terentev. Determination of welding speed in electron beam welding of thick components with continuous penetration. *Welding International*, 31, 2017. 10.1080/09507116.2016.1257243.
- [19] S. Lathabai. Comparison of keyhole and conventional gas tungsten arc welds in commercially pure titanium. page 299, Feb. 2001. doi:10.1016/S0921-5093(00)01408-8.
- [20] Copper and copper alloys. 2018.
- [21] T. W. Institute. Weldability of materials - copper and copper alloys.
- [22] En12163(2011) copper and copper alloys. rod for general purposes. 2011.
- [23] N. N. GmbH. Datasheet - cucr1zr.
- [24] P. I. Coutinho L. Joining processes. *Lecture Notes. Técnico University*.
- [25] A. D. C. B. Wisniewski J, Drezet J. Determination of the thermophysical properties of a cucr1zr alloy from liquid state down to room temperature. *International Journal of Material Forming*, 1: 1059–1062, 2008.
- [26] H. B. D. S. W. W. J. M. A. R. A. C. F. C. L. Aucott, D. Huang. A three-stage mechanistic model for solidification cracking during welding of steel. *Metallurgical and Materials Transactions*, 49: 1674–1682, 2018.
- [27] How to Avoid Cracking in Aluminum Alloys. URL <https://www.esabna.com/us/en/education/blog/how-to-avoid-cracking-in-aluminum-alloys.cfm>.
- [28] C. C. L. M. S. W. Durocher A, Ayrault D. Cucr1zr alloy hot cracking during electron beam welding. *Journal of Nuclear Materials*, pages 1208–1212, 2007.
- [29] J. N. Reddy. An introduction to the finite element method (third edition). *McGraw-Hill*, 2005.
- [30] L. F. M. N. L. Faria, P. Fernandes. Computational mechanics. resumos teóricos. 2017.
- [31] J. H. Lienhard. A heat transfer textbook. <https://ahtt.mit.edu/wp-content/uploads/2020/08/AHTTv510.pdf>.
- [32] T. B. A. L. F. Incropera, D. DeWitt. *Fundamentals of heat and mass transfer - Sixth edition*, volume 112. 2005.
-

- 
- [33] H. J. Yang Z, Fang Y. Numerical simulation of heat transfer and fluid flow during vacuum electron beam welding of 2219 aluminium girth joints. 175, 2020.
- [34] A. K. Lacki P. *Numerical simulation of the electron beam welding process*, volume 89. 2011.
- [35] T. Kik. Heat source models in numerical simulationsof laser welding. 2020.
- [36] S. N. e. A. P. G. Silva, C. Amado. Probabilidades e estatística. apontamentos teóricos. 2016.
- [37] J. M. Noble. Multiple linear regression and experimental design. *Lecture Notes. Linköping University*.
- [38] D. C. Montgomery and G. C. Runger. Applied statistics and probability for engineers. 2006.
- [39] S. M. Ross. Introduction to probability and statistics for engineers and scientists. 2009.
- [40] J. Martins. Identificação de sistemas. apontamentos teóricos. 2018.
- [41] M. Inc. Minitab. *Comput. Stat. Data Analysis*, Mar. 1983. doi: 10.1016/0167-9473(83)90065-8.
- [42] J. Antony. *Design of Experiments for Engineers and Scientists*. Elsevier Ltd, 2003. ISBN 9780750647090. doi: 10.1016/B978-0-7506-4709-0.X5000-5.
- [43] *Design of Experiments for Engineers and Scientists: Second Edition*. Elsevier Ltd, 2014. ISBN 9780080994178. doi: 10.1016/C2012-0-03558-2.
- [44] B. Durakovic. Design of experiments application, concepts, examples: State of the art. *Periodicals of Engineering and Natural Sciences*, 5(3), 2017. ISSN 23034521. doi: 10.21533/pen.v5i3.145.
- [45] Design of experiments: an overview and application example. *Medical Device and Diagnostic Industry*, 18(3), 1996. ISSN 0194844X.
- [46] C. C. and V. V. Support-vector networks. *Machine Learning*, 1995.
- [47] Y. B. Svm-induced dimensionality reduction and classification. *In proceedings of Second conference on intelligent computation technology and Automation*, pages 275–278, 2009.
- [48] G. A.J. and C. R.F. Support vector machine for hyperspectral remote sensing classification. *Advances in computer Assisted Recognition*, 1998.
- [49] A. V. Soman K.P. and L. R. Machine learning with svm and other kernel methods. *Prentice-Hall India*, 2009.
- [50] S. WANG, Y. HUANG, and L. ZHAO. Effects of different aging treatments on microstructures and mechanical properties of Al-Cu-Li alloy joints welded by electron beam welding. *Chinese Journal of Aeronautics*, 2018.
- [51] F. J. L. R. X. H. L. F. Q. B. Zhang W, Fu H. Influence of multi-beam preheating temperature and stress on the buckling distortion in electron beam welding. *Materials and Design*, 139:439–446, 2018.
-

- 
- [52] J. Fan, W. Zhang, B. Qi, and F. Liu. Influence of Multi-Beam Electron Beam Welding Technique on the Deformation of Ti6Al4V Alloy Sheet. *Xiyou Jinshu Cailiao Yu Gongcheng/Rare Metal Materials and Engineering*, 46:2417–2422, sep 2017. doi: 10.1016/s1875-5372(17)30208-4.
- [53] G. A. B. M. R. M. Bakir N, Artinov A. Numerical simulation on the origin of solidification cracking in laser welded thick-walled structures. *Metals*, 8(6), jun 2018. doi: 10.3390/MET8060406.
- [54] M. Chiumenti, M. Cervera, N. Dialami, B. Wu, L. Jinwei, and C. Agelet de Saracibar. Numerical modeling of the electron beam welding and its experimental validation. *Finite Elements in Analysis and Design*, 121:118–133, nov 2016. doi: 10.1016/j.finel.2016.07.003.
- [55] P. Lacki and K. Adamus. Numerical simulation of the electron beam welding process. volume 89, pages 977–985, jun 2011. doi: 10.1016/j.compstruc.2011.01.016.
- [56] R. SINGH, S. SINGH, P. K. KANIGALPULA, and J. S. SAINI. Electron beam welding of precipitation hardened CuCrZr alloy: Modeling and experimentation. 30(8):2156–2169, aug 2020. ISSN 22103384. doi: 10.1016/S1003-6326(20)65368-7.
- [57] M. Arab and M. Zemri. Optimization of process parameters on friction stir welding of aa 6082-t6 butt joints using taguchi method. *Materials Today: Proceedings*, Jan. 2020. doi: 10.2478/mme-2018-0107.
- [58] D. Sathishkumar and A. D. Das. Investigations on effect of process parameters on gtaw of aluminium alloy welding using full factorial design technique. *Materials Today: Proceedings*, Jan. 2020. doi: 10.1016/j.matpr.2020.05.624.
- [59] V. K. H. Singh and J. Kapoor. Multi-response optimization of wedm process parameters during the fabrication of microchannels for industrial applications. *Mater. Today Proc.*, Jul. 2020. doi: 10.1016/j.matpr.2020.06.134.



# Appendix A

## Technical Datasheets

### A.1 EB Machine

Important benchmarks regarding the EBW machine at TU Graz can be found in Tables A.1, A.2 and A.3. The EB machine was manufactured by pro-beam. It is the “Universal-chamber machine EBG 45-150 K14” model. This machine type offers a wide range of applications. It is especially appropriate for research and for welding prototypes. The equipment can be seen in Figure A.1.

Electron Beam Gun	
Power	45kW
High Voltage	150kV
Beam Current	0,1 - 300 mA
Beam Oscillation	1°/μs

Table A.1: EBW-Gun benchmarks.

Chamber	
Volume	1,4m <sup>3</sup>
Table Feed Rate	0,5 - 100 mm/s

Table A.2: EBW-Chamber benchmarks.

Vacuum	
Evacuation Time	< 6min
EB Gun	$\leq 5 \cdot 10^{-5}$ mbar
Chamber	$\leq 5 \cdot 10^{-3}$ mbar

Table A.3: EBW-Vacuum benchmarks.



Figure A.1: EB-Machine at TU Graz.